

Adaptive UAV-Assisted Hierarchical Federated Learning: Optimizing Energy, Latency, and Resilience for Dynamic Smart IoT

Xiaohong Yang, Minghui Liwang, *Member, IEEE*, Liqun Fu, *Senior Member, IEEE*, Yuhan Su, Seyyedali Hosseinalipour, *Member, IEEE*, Xianbin Wang, *Fellow, IEEE*, Yiguang Hong, *Fellow, IEEE*

Abstract—Hierarchical Federated Learning (HFL) enhances the conventional Federated Learning (FL) paradigm by introducing intermediate aggregation layers, facilitating distributed learning in geographically dispersed environments. A key application of HFL lies in smart Internet of Things (IoT) systems, including remote monitoring and battlefield operations, where cellular connectivity is often unavailable. In such scenarios, UAVs can act as mobile aggregators, dynamically providing connectivity to terrestrial IoT devices. Subsequently, this paper investigates an HFL architecture enabled by energy-constrained, dynamically deployed UAVs that are susceptible to communication disruptions. We propose a novel approach to minimize global training costs in such environments by formulating a joint optimization problem that integrates learning configuration, bandwidth allocation, and IoT device-to-UAV association, ensuring timely global aggregation before UAV disconnections and redeployments. The problem explicitly captures the dynamic nature of IoT devices and their intermittent connectivity to UAVs and is shown to be NP-hard. To address its complexity, we decompose the problem into three interrelated subproblems. First, we optimize learning configuration and bandwidth allocation using an augmented Lagrangian function to reduce training costs. Second, we introduce a device fitness score that accounts for data heterogeneity (via Kullback-Leibler divergence), device-to-UAV proximity, and computational resources, leveraging a Twin Delayed Deep Deterministic Policy Gradient (TD3)-based algorithm for adaptive device-to-UAV assignment. Third, we develop a low-complexity two-stage greedy strategy for UAV redeployment and global aggregator selection, ensuring efficient model aggregation despite UAV disconnections. Experiments on real-world datasets validate the effectiveness of our approach in terms of cost reductions and robust performance under communication disruptions.

Index Terms—Hierarchical federated learning, Unmanned aerial vehicles, Network optimization, Deep reinforcement learning.

1 INTRODUCTION

As the demand for machine learning tasks in the Internet of Things (IoT) ecosystem grows, traditional centralized ML approaches, which rely on transferring raw data to a central server, face significant challenges, including privacy concerns, security risks, and inefficiencies in leveraging distributed data across diverse network entities [1], [2]. Federated Learning (FL) addresses these challenges by aggregating locally trained models from distributed devices in a cloud server without requiring the sharing of private data, making it particularly enticing for smart IoT applications [3]–[6]. However, as the number of devices increases, direct communication between a central cloud server and all devices becomes impractical due to frequent link outages, high latency, and congestion over the backhaul networks [7]–[9]. To overcome these limitations, Hierarchical Federated Learning (HFL) introduces middle-layer aggregators, such as edge servers, to the conventional model training architecture of FL, enabling near-device model aggregations. In HFL, devices connect to edge servers based on criteria like geographical proximity or data

similarity. Devices' local models are then aggregated at the edge servers before being sent to the cloud for global aggregation [10]–[13]. This hierarchical structure significantly enhances the communication efficiency and the scalability of distributed model training across IoT devices, making it particularly suitable for large-scale IoT networks with geographically dispersed devices.

1.1 Motivation and Challenges

A key application of HFL is in smart IoT systems operating in environments where cellular connectivity is often unavailable or unreliable, such as remote environmental monitoring, disaster response, and battlefield operations [14], [15]. In such environments, direct access of the IoT devices to the edge servers via base stations or roadside units is often impractical. To address these constraints, Unmanned Aerial Vehicles (UAVs) can be deployed as flexible and adaptable model aggregators [16], enabling UAV-assisted HFL. Recent studies in this domain include *Huang et al.* [17], which provided a framework for HFL in Space-Air-Ground Integrated Networks (SAGINs) with UAV acting as edge servers; *Zou et al.* [18], which optimized energy efficiency in HFL scenarios where UAVs can be re-charged periodically; *Xu et al.* [19], which proposed clustering mechanisms to incentivize UAVs to participate in FL tasks; *Ruslan et al.* [20], which developed UAV-assisted HFL for wireless networks to counteract the impact of unreliable channels; *X. Song et al.* [21], which proposed an HFL algorithm for optimizing computation offloading in SAGINs composed of UAVs through a deep Q-network (DQN)-based approach.

While the aforementioned works have made notable contributions to the field, we identify two critical challenges that remain

Xiaohong Yang and Liqun Fu are with the School of Informatics, Xiamen University, Fujian, China. Minghui Liwang and Yiguang Hong are with the Department of Control Science and Engineering, the National Key Laboratory of Autonomous Intelligent Unmanned Systems, and also with Frontiers Science Center for Intelligent Autonomous Systems, Ministry of Education, Tongji University, Shanghai, China. Yuhan Su is with the School of Electronic Science and Engineering, Xiamen University, Xiamen, China. Seyyedali Hosseinalipour is with the department of Electrical Engineering, University at Buffalo-SUNY, Buffalo, NY, USA. Xianbin Wang is with the Department of Electrical and Computer Engineering, Western University, Ontario, Canada. Corresponding author: Minghui Liwang.

underexplored: (i) *IoT Device Dynamics and Heterogeneity* and (ii) *UAV's Energy Constraints and Reliability*.

Challenge 1. IoT Device Dynamics and Heterogeneity: Ineffective tuning of the frequency of local and edge iterations, resource allocation, and the local/global model aggregation topology, coupled with IoT device mobility, data heterogeneity, and computational and communication constraints, significantly hinders the efficiency and convergence of global models in UAV-assisted HFL. These challenges make it difficult to achieve consistent, efficient, and optimal model performance in dynamic and heterogeneous smart IoT environments.

Several efforts have aimed to address these challenges. *Liu et al.* [22] optimized the number of local and edge iterations and determined device-to-edge (D2E) associations based on signal-to-noise ratio (SNR) in HFL. *Qi et al.* [23] developed a learning-based synchronization scheme to improve resource efficiency and accuracy of HFL, while *Li et al.* [24] incorporated the joint impact of model accuracy, resource availability, and energy consumption to optimize the operations in HFL. Similarly, *Dong et al.* [25] introduced a multi-metric fuzzy logic-based device selection scheme for HFL. Although these works are mostly focused on terrestrial HFL frameworks, their methods continue to be effective in addressing the device heterogeneity within UAV-assisted HFL architectures. Furthermore, several studies have directly studied UAV-assisted HFL, such as *Tong et al.* [26] who optimized UAV-to-edge device association based on resource allocation and location of edge devices and UAVs. Also, *R. Khelif et al.* [27] proposed UAV-to-device association based on the uplink delay between IoT devices and UAVs. Despite these advancements, most existing approaches rely on fixed strategies for device-to-UAV association, resource allocation, and learning configuration, which fail to accommodate the inherent dynamics of smart IoT environments. Specifically, in real-world deployments, IoT devices exhibit unpredictable mobility, and the collective data distribution of devices covered by each UAV fluctuates over time due to device arrivals and departures. As a result, existing methods often struggle to adapt to these evolving conditions, leading to inefficient device selection, suboptimal resource allocation, and prolonged model convergence — ultimately degrading the overall performance of UAV-assisted HFL. To overcome these limitations, a fundamental paradigm shift is required — moving towards adaptive and intelligent mechanisms for device-to-UAV association, resource allocation, and learning configuration that can dynamically respond to real-time network variations. This critical need serves as a motivation for our proposed framework, which is designed to optimize resource (in terms of energy and delay) efficiency, improve learning performance, and enhance model convergence in dynamic UAV-assisted HFL environments.

Challenge 2. UAV's Energy Constraints and Reliability: The limited energy supply of UAVs adds another layer of complexity to UAV-assisted HFL, as UAV shutdowns and downtimes during training can severely affect the learning process and model convergence. Consequently, a body of literature has emerged focusing on reducing the energy consumption of UAVs in HFL. For instance, [28] and [29], aimed to minimize the UAV energy consumption and mission delays in HFL. Also, *Wang et al.* [30] proposed a battery re-charging methodology for UAVs in the HFL architecture. Despite their notable contributions, these studies primarily address UAVs' energy efficiency and mission sustainability, but they fail to consider the broader impact of UAV disconnections and downtimes on the overall HFL process. Specifically, they overlook

the loss of model updates when UAVs disconnect from IoT devices, leading to gaps in global aggregation and degraded model performance. Additionally, in most of these approaches, UAVs operate in fixed positions, limiting their ability to adapt to dynamic network conditions and IoT device mobility. As a result, IoT devices that could have communicated with a now-disconnected UAV are excluded from participation in global training, leading to underutilized resources and inefficient learning progress. Thus, beyond merely reducing UAV energy consumption, it is imperative to develop adaptive mechanisms that mitigate the impact of UAV disconnections and downtimes on HFL training. This crucial aspect has been largely overlooked in prior research, yet it is essential for ensuring robust, uninterrupted learning in dynamic UAV-assisted HFL environments. Addressing this limitation serves as another core motivation behind this work, driving the need for a framework that jointly optimizes UAV energy management, adaptive redeployment, and model aggregation topology.

1.2 Overview and Summary of Contributions

Building on the above discussions, this paper explores a UAV-assisted HFL architecture tailored for dynamic and heterogeneous IoT environments. In this architecture, UAVs, constrained by limited energy supply, can simultaneously function as edge/intermediate and global/terminal aggregators, adjusting their positions based on dynamic IoT devices' configuration. Also, during the HFL training process, each UAV can autonomously adapt its device association strategy based on the characteristics and the heterogeneous devices within its coverage area.

The key contributions of this work are summarized as follows:

- We explore a relatively underexamined UAV-assisted HFL architecture for IoT networks, where energy-constrained UAVs may experience downtimes and intermittent communication disruptions. Additionally, we account for the computation and communication heterogeneity of IoT devices, as well as their mobility/dynamics, allowing them to transition across different UAV coverage regions throughout the HFL process.
- To ensure efficient model training in this dynamic and heterogeneous IoT environment, we formulate an optimization problem that balances HFL training delay and energy consumption while preserving model accuracy and mitigating the impact of UAV disconnections and downtimes. We unveil the NP-hard nature of this problem, and then decompose it into three interdependent subproblems and develop complementary solutions for them.
- In the first subproblem, we aim to optimize the learning configuration of IoT devices, specifically focusing on the number of local iterations and bandwidth allocation among devices connected to UAVs. The objective is to minimize local training costs in terms of both time and energy. To achieve this, we design an optimization algorithm leveraging an augmented Lagrangian function with a penalty term, ensuring convergence to the optimal solution.
- In the second subproblem, we address finding effective device-to-UAV associations through an intelligent approach powered by Twin Delayed Deep Deterministic Policy Gradient (TD3). Specifically, we introduce a model difference score, which leverages Kullback-Leibler Divergence (KLD) to quantify data heterogeneity across devices. Additionally, we incorporate key factors such as device-to-UAV distance and device computing resources to compute a fitness score for optimal device-to-UAV pairings. To systematically model this problem, we formulate it as a Markov Decision Process (MDP) and tailor a TD3-based reinforcement learning solution methodology to it.

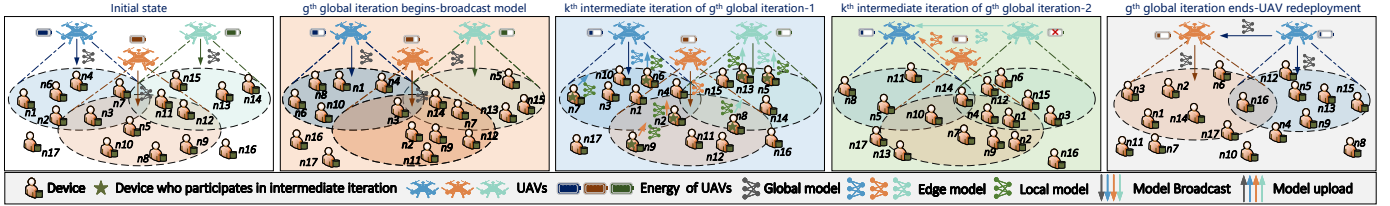


Fig. 1: A schematic of HFL architecture over smart IoT of our interest with energy-constrained UAVs and dynamic devices that move between various UAV’s coverage areas.

- Finally, in the third subproblem, we develop a UAV energy inspection and location optimization mechanism to determine the appropriate roles of UAVs — whether they should function as intermediate aggregators or as the final global model aggregators. This decision-making process helps establishing optimal model aggregation schedules, and mitigating the risk of data loss due to interruptions in device-to-UAV and UAV-to-UAV communication links. In this framework, based on its role, each UAV dynamically adjusts its position to maximize device coverage, thereby reducing both device-to-UAV and UAV-to-UAV communication costs. To efficiently solve this subproblem, we propose a low-complexity dual-stage heuristic algorithm.
- Extensive experiments on various real-world datasets demonstrate that our proposed method can lead to notable training cost reductions in terms of energy and delay while ensuring a commendable convergence rate of the trained model in HFL. Furthermore, compared to existing approaches, our method can better prevent the loss of device model parameters and delays in global model convergence caused by device-to-UAV link interruptions and UAV downtimes.

2 SYSTEM OVERVIEW

2.1 IoT Device and UAV Operations

We consider a dynamic and heterogeneous IoT network with multiple energy-constrained UAVs collected by the set $\mathcal{M} = \{1, \dots, M\}$, and multiple terrestrial IoT devices collected by the set $\mathcal{N} = \{1, \dots, N\}$, which can move across the coverage regions of the UAVs. In a nutshell, the procedure of HFL in our scenario of interest can be summarized as follows:

- **Part 1. Initial Model Broadcast and Device Selection:** In the first part of our learning methodology, the UAV designated as the global model aggregator — detailed in parts 2 and 3 below — distributes the latest global model to all UAVs in the network (in the first training round, the selection of the global model aggregator is random, and the initial model is randomly initialized at this UAV). Each UAV then broadcasts the global model to all devices within its communication range. Afterwards, devices are selected for local training based on adaptive thresholds and device fitness scores, which consider data relevance and quality, communication and computational capabilities, and proximity to the UAVs. The selected devices use their local datasets to train their models via stochastic gradient descent (SGD) iterations, with their local models initialized by the global model. Once local training is completed, the devices transmit their updated local models back to their assigned UAVs, triggering the second phase of our methodology, which is detailed in the following.
- **Part 2. Intermediate Aggregation and UAV Energy Evaluation:** Upon receiving the updated models from devices, each UAV performs intermediate aggregation to generate an updated intermediate local model. Following this step, UAVs assess their energy status to determine the next course of action, leading to one of two possible scenarios:

Case 1: If all UAVs have sufficient energy to support additional intermediate aggregations, they broadcast their aggregated intermediate models to their covered devices, initiating the next round of local training. To prevent bias in the intermediate models, even when all UAVs have adequate energy, a UAV is periodically selected and deployed for global aggregation after a predefined number of edge aggregation rounds.

Case 2: If any UAV lacks sufficient energy to continue intermediate aggregations, a UAV is selected as the global aggregator, and all UAVs upload their intermediate models to this UAV for global model aggregation. Additionally, UAVs with depleted energy exit the network and return to their base nodes for recharging.

In either case, once the global aggregation is conducted, the third part of our methodology is triggered as detailed below.

- **Part 3. Global Aggregation and UAV Relocation:** Once a global aggregation is triggered, the designated global aggregator UAV disseminates the updated global model to all active UAVs in the network. These UAVs may then relocate to maximize coverage and enhance model performance, particularly in cases where some UAVs have exited the network for recharging. This repositioning allows UAVs and IoT devices to continue participating in subsequent intermediate and global aggregation rounds, ensuring the uninterrupted progression of the HFL process.

This cycle — comprising local training and intermediate iterations, UAV energy evaluations, and global aggregations — repeats until the global model converges to the desired performance level. Henceforth, we use k and g to denote a specific intermediate and global aggregation round, respectively.

Remark 1 (UAVs’ Departures and Arrivals). *In this paper, we focus on the operational procedures triggered by UAV disconnections and downtimes, such as device-to-UAV re-association, bandwidth reallocation, and UAV repositioning. These procedures are crucial for maintaining system performance and ensuring continuity of training despite UAV failures. Although UAVs may recharge and subsequently rejoin the FL process, we do not explicitly detail the rejoining procedures in this work. This is because the operations required when a UAV re-enters the network — including re-initialization of device associations, bandwidth adjustments, and potential repositioning — mirror the operations performed when a UAV disconnects. As such, to avoid redundancy and maintain conciseness, we have omitted a separate explanation of these procedures upon UAV rejoining.*

2.2 Modeling of IoT Devices and UAVs

Modeling of Devices and UAVs: We presume that each terrestrial IoT device $n \in \mathcal{N}$ has a local dataset denoted by $\mathcal{D}_n = \{(x_j, y_j) | 1 \leq j \leq |\mathcal{D}_n|\}$, where x_j and y_j refer to the feature vector and label of the j^{th} local data point, respectively. We denote the set of IoT devices covered by active UAV $m \in \mathcal{M}$ during the g^{th} global aggregation as $\mathcal{N}_{m|g}^{\text{Cov}}$. We also denote the subset of IoT devices in the coverage of UAV m that are selected/chosen

and participate in each round of model training as $\mathcal{N}_{m';[g]}^{\text{Sel}}$. We further denote the coordinates of each device n positions during global aggregation g as $\mathbf{p}_{n;[g]} = (\mathbf{p}_{n;[g]}(x), \mathbf{p}_{n;[g]}(y))$, where $\mathbf{p}_{n;[g]}(x)$ and $\mathbf{p}_{n;[g]}(y)$ denote the x and y locations of the device, respectively. We assume that the locations of devices remain stationary within each global aggregation round, although they may change between successive rounds. Furthermore, between different global iterations, each device has a certain probability of remaining within the coverage area of its current UAV or transitioning to the coverage area of another UAV.

Additionally, the location of each UAV m during global aggregation round g is denoted as $\mathbf{p}_{m;[g]} = (\mathbf{p}_{m;[g]}(x), \mathbf{p}_{m;[g]}(y), \mathcal{H})$, where \mathcal{H} represents the altitude at which the UAVs are deployed. This spatial representation plays a crucial role in network optimization within our UAV-assisted HFL framework. We also consider a realistic scenario where each UAV m has a limited battery capacity, denoted by E_m^{Batt} . The battery depletes at a rate of \overline{p}_m (in Watts) while the UAV is hovering in the air. Additionally, each UAV can relocate at a specific moving speed in the air, represented by V_m . These factors influence the UAV's operational time, mobility constraints, and overall network sustainability in our UAV-assisted HFL framework.

Communication Models in UAV-Assisted HFL: In our HFL scenarios of interest, three types of model transfers occur: device-to-UAV (D2U), UAV-to-device (U2D), and UAV-to-UAV (U2U) communications. Due to the sequential nature of the local training, intermediate aggregation, and global aggregation processes, these communications occur in separate phases and do not interfere with each other. Specifically, D2U transmissions never take place when U2U communications are happening, and similarly, U2D transmissions are scheduled separately from both D2U and U2U transmissions. Furthermore, in each mode of communication, bandwidth allocation will later be designed to ensure non-overlapping frequency resources among devices and UAVs, removing the impact of interference in our analysis.

In particular, for D2U communication between device n and active UAV m , the data rate during the g^{th} global iteration is

$$r_{n \rightarrow m;[g]}^{\text{D2U}} = B_{m,n;[g]}^{\text{D2U}} \log_2 \left(1 + S_{n \rightarrow m;[g]}^{\text{D2U}} \right), \quad (1)$$

where the signal-to-noise ratio (SNR) $S_{n \rightarrow m;[g]}^{\text{D2U}}$ is

$$S_{n \rightarrow m;[g]}^{\text{D2U}} = \frac{p_n^{\text{D2U}} d_{m,n;[g]}^{-\alpha_{\text{D2U}}}}{N_0 B_{m,n;[g]}^{\text{D2U}}}. \quad (2)$$

Here, $B_{m,n;[g]}^{\text{D2U}}$ represents the amount of uplink bandwidth of UAV m allocated to device n , p_n^{D2U} denotes the transmit power of device n , α_{D2U} captures the D2U link path loss exponent, and N_0 is the noise power spectral density. Similarly, for U2D communication, the downlink data rate is given by

$$r_{m \rightarrow n;[g]}^{\text{U2D}} = B_{m,n;[g]}^{\text{U2D}} \log_2 \left(1 + S_{m \rightarrow n;[g]}^{\text{U2D}} \right), \quad (3)$$

where the corresponding SNR is

$$S_{m \rightarrow n;[g]}^{\text{U2D}} = \frac{p_m^{\text{U2D}} d_{m,n;[g]}^{-\alpha_{\text{U2D}}}}{N_0 B_{m,n;[g]}^{\text{U2D}}}. \quad (4)$$

Here, $B_{m,n;[g]}^{\text{U2D}}$ represents the downlink bandwidth allocated to device n , p_m^{U2D} denotes the transmit power of UAV m , and α_{U2D} captures the U2D link path loss exponent.

Finally, for U2U communication, the data rate is given by

$$r_{m \rightarrow m';[g]}^{\text{U2U}} = B_{m,m';[g]}^{\text{U2U}} \log_2 \left(1 + S_{m \rightarrow m';[g]}^{\text{U2U}} \right), \quad (5)$$

where the corresponding SNR is:

$$S_{m \rightarrow m';[g]}^{\text{U2U}} = \frac{p_m^{\text{U2U}} d_{m,m';[g]}^{-\alpha_{\text{U2U}}}}{N_0 B_{m,m';[g]}^{\text{U2U}}}. \quad (6)$$

Here, $B_{m,m';[g]}^{\text{U2U}}$ represents the bandwidth allocated for communication between UAV m and UAV m' , and α_{U2U} captures the U2U link path loss exponent.

3 ENERGY-CONSTRAINED UAV-ASSISTED HFL OVER DYNAMIC IoT

We let $K_{[g]}$ denote the number of intermediate aggregations performed during global aggregation g . In our scenario, $K_{[g]}$ is dynamically tuned based on the interplay between network configurations (e.g., remaining UAV battery levels and delays in model transfers from IoT devices to UAVs) and ML performance. In Section 3.3.2, we address these factors jointly and determine the optimized value of $K_{[g]}$ for each global aggregation g .

To capture the roles and status of UAVs in our HFL scenario, we define $\mathcal{M}_{[g]}$ as the set of UAVs that are *active* in model transfer and local aggregation during global aggregation g . Also, we introduce the binary variables $\phi_{[g]} \in \{0, 1\}$ and $X_{m;[g]} \in \{0, 1\}$ to indicate UAV disconnections and global aggregator selection, respectively. Specifically, $\phi_{[g]} = 1$ indicates that at least one UAV does not have enough battery to continue staying the network during global round g , and $X_{m;[g]} = 1$ signifies that UAV m has been selected as the global aggregator for global round g .

3.1 Energy-Constrained UAV-assisted HFL

We next mathematically formalize the procedures of our UAV-assisted HFL scenario. This formalization begins with defining the processes that take place at the IoT devices, including local training, model updates, and communication with UAVs. We then describe the role of UAVs serving as intermediate aggregators, which are responsible for collecting local models and performing intermediate aggregations. Finally, we define the role of the UAV selected as the global model aggregator, which collects intermediate models from UAVs and performs the final global aggregation.

(A) Device Operations: During the HFL model training period, each device aims to minimize its local loss function. In particular, the local loss function for device n under an arbitrary model parameter w is given by

$$L_n(w) = \sum_{j \in \mathcal{D}_n} l_j(w), \quad (7)$$

where l_j represents the loss for the j^{th} local data point, commonly defined using cross-entropy loss or other relevant error metrics.

To minimize its local loss function during the local learning iterations, each IoT device maintains a local model, denoted as $w_{n;[g,k,h]}^{\text{Dev}}$, where the indices represent the specific global aggregation round g , intermediate aggregation round k , and local iteration h . This local model is synchronized with the received global model at the beginning of each global aggregation round, ensuring alignment with the latest updates from the network, as $w_{n;[g,0,0]}^{\text{Dev}} = w_{[g-1]}$, where $w_{[g-1]}$ is the global model from the previous round. Also, at the beginning of each intermediate aggregation round k , the local model at device n is reinitialized with the latest model received from its assigned UAV m as $w_{n;[g,k,0]}^{\text{Dev}} = w_{m;[g,k-1]}^{\text{UAV}}$, where $w_{m;[g,k-1]}^{\text{UAV}}$ is the intermediate model aggregated by UAV m , which covers device n .

Subsequently, during local training, each device updates its local model using SGD iterations as follows:

$$w_{n;[g,k,h]}^{\text{Dev}} = w_{n;[g,k,h-1]}^{\text{Dev}} - \eta \widetilde{\nabla} L_n(w_{n;[g,k,h-1]}^{\text{Dev}}), \quad (8)$$

where η is the learning rate, and $\tilde{\nabla}$ represents the stochastic gradient. In particular, the stochastic gradient is computed as the average loss over the sampled mini-batch $B_{n;[g,k,h]}$ from the local dataset \mathcal{D}_n as $\tilde{\nabla} L_n(w_{n;[g,k,h-1]}^{\text{Dev}}) = \frac{1}{|B_{n;[g,k,h]}|} \sum_{j \in B_{n;[g,k,h]}} \nabla l_j(w_{n;[g,k,h-1]}^{\text{Dev}})$. Assuming that each device performs H SGD iterations per local training phase, the final trained model at device n , denoted as $w_{n;[g,k,H]}^{\text{Dev}}$, is transmitted to its assigned UAV. This updated model is then used to compute the next intermediate model at the UAV $w_{m;[g,k]}^{\text{UAV}}$, as detailed below.

(B) Intermediate Aggregations: After the reception of the local models of the IoT devices contained in the set $\mathcal{N}_{m;[g]}^{\text{Sel}}$ at each active UAV m , this UAV obtains its intermediate model as follows:

$$w_{m;[g,k]}^{\text{UAV}} = \sum_{n \in \mathcal{N}_{m;[g]}^{\text{Sel}}} |\mathcal{D}_n| w_{n;[g,k,H]}^{\text{Dev}} / |\mathcal{D}_{m;[g]}^{\text{Sel}}|, \quad (9)$$

where $w_{n;[g,k,H]}^{\text{Dev}}$ represents local model parameters received from device $n \in \mathcal{N}_{m;[g]}^{\text{Sel}}$. Besides, $|\mathcal{D}_{m;[g]}^{\text{Sel}}| = \sum_{n \in \mathcal{N}_{m;[g]}^{\text{Sel}}} |\mathcal{D}_n|$ represents the total size of datasets of all devices covered by UAV m . This model is then sent back to the devices covered by the UAV and is used to synchronize their local models, initiating the next round of local training. After several repetitions of the above procedure, when $k = K_{[g]}$, where the value of $K_{[g]}$ will be later optimized according to UAVs' battery levels and model performance, each active UAV m sends its intermediate model $w_{m;[g,K_{[g]}]}^{\text{UAV}}$ to the UAV designated as the global model aggregator, which computes the next global model $w_{[g]}$ as described next.

(C) Global Aggregations: After the reception of models from UAVs at the UAV m that was designated to be the global model aggregator (i.e., $X_{m;[g]} = 1$), this UAV combines the received models to form the next global model as follows:

$$w_{[g]} = \sum_{m \in \mathcal{M}_{[g]}} |\mathcal{D}_{m;[g]}^{\text{Sel}}| w_{m;[g,K_{[g]}]}^{\text{UAV}} / |\mathcal{D}_{[g]}|, \quad (10)$$

where $|\mathcal{D}_{[g]}| = \sum_{m \in \mathcal{M}_{[g]}} |\mathcal{D}_{m;[g]}^{\text{Sel}}|$ indicates the combined size of datasets of all devices engaged in global aggregation g . Further, we consider that the training ends at global aggregation g once two consecutive global models satisfy the following condition:

$$\|w_{[g]} - w_{[g-1]}\| \leq \delta, \quad (11)$$

where $\|\cdot\|$ represents Euclidean 2-norm, and δ is a small positive value used to control the convergence criterion. If the convergence criterion is not met, $w_{[g]}$ is broadcasted across the UAVs and the next round of device operations starts. The processes that take place during our designed HFL are summarized in Alg. 1.

3.2 Multi-Metric Device Evaluation Scores and Device-to-UAV Associations

In dynamic and heterogeneous scenarios, multiple factors influence device-to-UAV association, including the varying distances between devices and UAVs, as well as computational resources available of the devices. More importantly, previous studies [31], [32] have demonstrated that the diversity in device data distribution significantly impacts global model convergence. Specifically, in our context of interest, intermediate aggregations that involve devices with more diverse data distributions (i.e., greater variations in data characteristics) connected to each UAV tend to enhance global model convergence.

Given these considerations, quantifying devices' values/benefits across multiple dimensions is essential for optimizing device-to-UAV association. To achieve this, we propose the following fitness score between each device n and UAV m for each global round g that quantifies the value of a device for UAV association

Algorithm 1: The HFL procedure of our interest

```

1 Input :  $\mathcal{K}^{\text{Max}}, H, \eta, E_{m;[0]}^{\text{Batt}}$ ;
2 Output :  $w_{[g]}$ ;
3 Initialization :  $w_n = w_{[0]}$ ;
4 if the global model parameter changes does not satisfy (11) then
5   Role 1. process: // running at each online UAV
6   for each edge communication round  $k = \{1, 2, \dots, \mathcal{K}^{\text{Max}}\}$  do
7     for each UAV  $m \in \mathcal{M}_{[g]}$  do
8       Obtain  $\mathcal{N}_{m;[g]}^{\text{Sel}}$  through Alg. 3.
9       Device process: // running at each device
10      for  $n \in \mathcal{N}_{m;[g]}^{\text{Sel}}$  in parallel do
11        Refresh the device's local model parameters:
12         $w_{n;[g,k,0]}^{\text{Dev}} \leftarrow w_{m;[g,k-1]}^{\text{UAV}}$ .
13        for  $h = \{1, 2, \dots, H\}$  do
14          Update  $w_{n;[g,k,h]}^{\text{Dev}}$  based on (8).
15        Upload  $w_{n;[g,k,H]}^{\text{Dev}}$  to the associated UAV.
16      UAV aggregation of model parameters from all devices
17      according to (9).
18   Role 2. process: // running at global aggregator UAV
19   for  $m \in \mathcal{M}_{[g]}$  do
20     Move to the appropriate position based on Alg. 4.
21     According to Alg. 4, select global aggregator UAV and
22     aggregate global model based on (10).
23     Global aggregator UAV broadcast global model  $w_{[g]}$  to online
24     UAVs and they continue to broadcast to devices.
25     Update the battery capacity  $E_{m;[g]}^{\text{Batt}}$ .

```

based on three key aspects: data distribution diversity, distance to the UAV, and available computing resources:

$$\alpha_{m,n;[g]} = \lambda_1 S_{m,n;[g]}^{\text{Sim}} + \lambda_2 S_{m,n;[g]}^{\text{Dis}} + \lambda_3 S_{m,n;[g]}^{\text{Fre}}, \quad (12)$$

where $\lambda_1, \lambda_2, \lambda_3$ are positive weighting coefficients, and $\lambda_1 + \lambda_2 + \lambda_3 = 1$. Besides, $S_{m,n;[g]}^{\text{Sim}}$ represents the *data distribution similarity score*, evaluating the relevance and diversity of device n dataset to the rest of the devices covered by UAV m , $S_{m,n;[g]}^{\text{Dis}}$ denotes the *distance score*, capturing the proximity of device n to UAV m , and $S_{m,n;[g]}^{\text{Fre}}$ measures *computing resources*, reflecting the processing capability of device n relative to the rest of the devices covered by UAV m in terms of its CPU frequency availability denoted by f_n .

Among the above three parameters, measuring differences in data distribution among devices is challenging, especially in HFL setting where devices do not share their private data with the UAVs. To address this, we introduce a model difference score based on Kullback-Leibler Divergence (KLD), denoted as $R_{m,n;[g]}$, to quantify the divergence between the data distribution of device n and the rest of the devices covered by UAV m . In particular, to compute this model difference score, we first assign a personalized model to each UAV. For UAV m , the assigned personalized model is represented as v_m^{Per} , which is trained on the UAVs' limited assigned local dataset. The assignment process involves distributing a limited number of the data points among UAVs. Such an assumption on having limited number of datapoints at the network edge is also presumed in [33]. Before each round of global aggregation, UAVs broadcast their personalized models to devices. Each device then computes a KLD-based model difference score, comparing the outputs of the personalized model received from the UAV with its own local model, using a small batch of datapoints from its dataset (i.e., $\mathcal{D}_n^{\text{Small}}$), where a higher model difference score indicates greater divergence in data distributions. In particular, the model difference score for device n under the coverage of UAV m is defined as:

$$R_{m,n;[g]} = \lambda_4 \sum_{j \in \mathcal{D}_n^{\text{Small}}} \Phi(v_m^{\text{Per}}, x_j) \log \frac{\Phi(v_m^{\text{Per}}, x_j)}{\Phi(w_{n;[g-1]}^{\text{Dev}}, x_j)}, \quad (13)$$

where x_j represents the local sample of the j^{th} input, $\Phi(v_m^{\text{Per}}, x_j)$ corresponds to the pre-softmax output of the UAV's personalized model, and $\Phi(w_{n;[g-1]}^{\text{Dev}}, x_j)$ is the pre-softmax output of the local model trained on the device. The parameter λ_4 is a hyperparameter that balances the impact of data and model differences. Consequently, UAVs prioritize selecting devices with higher model difference scores for participation in model training as those often have the highest diversity of data.

Subsequently, to compute (12), we normalize $R_{m,n;[g]}$, $d_{m,n;[g]}$ and f_n to obtain $S_{m,n;[g]}^{\text{Sim}} = R_{m,n;[g]}/R_{m;[g]}^{\text{Max}}$, $S_{m,n;[g]}^{\text{Dis}} = d_{m,n;[g]}^{\text{Min}}/d_{m,n;[g]}$, $S_{m,n;[g]}^{\text{Fre}} = f_n/f_{m;[g]}^{\text{Max}}$, where $R_{m;[g]}^{\text{Max}}$, $d_{m;[g]}^{\text{Min}}$, $f_{m;[g]}^{\text{Max}}$ represent the maximum model difference, the minimum distance between UAV and device, and the maximum clock frequency of the computing processor, respectively, among all devices within the coverage area of UAV m in the g^{th} round of global iteration.

After obtaining the above parameters, to ensure that only the most relevant devices contribute to the learning process, each computed fitness score in (12) is compared against an adaptive selection threshold, denoted by $\beta_{m;[g]}$. In particular, a device n under the coverage of active UAV m (i.e., $n \in \mathcal{N}_{m;[g]}^{\text{Cov}}$) is selected for participation in model training following the rule below

$$\begin{cases} \alpha_{m,n;[g]} \geq \beta_{m;[g]}, & n \in \mathcal{N}_{m;[g]}^{\text{Sel}}, \\ \text{otherwise,} & n \notin \mathcal{N}_{m;[g]}^{\text{Sel}}, \end{cases} \quad (14)$$

where the adaptive threshold $\beta_{m;[g]}$ is dynamically adjusted and later optimized in our problem formulation based on the network environment, including factors such as device mobility patterns, computational load, and communication constraints. Devices that satisfy this condition form the set of successfully selected participants under the coverage of each UAV m .

3.3 Modeling of Delay and Energy Costs

In this section, we first model the delay and energy consumption associated with model training and transfers on IoT devices, followed by the energy consumption of UAVs during hovering and information exchanges. Finally, we obtain the total energy and delay costs of our UAV-assisted HFL scenario of interest.

3.3.1 Delay and Energy Consumption of IoT Devices

At each global aggregation g , the model training latency of device n during each intermediate aggregation is given by $t_n^{\text{Cmp}} = H t_n^{\text{Unit}}$, where t_n^{Unit} represents the unit time taken by device n to complete one round of local training, that is,

$$t_n^{\text{Unit}} = t^{\text{Fix}} + \varphi_n c_n |\mathcal{D}_n| / f_n, \quad (15)$$

where $\varphi_n \in (0, 1]$ captures the fraction of datapoints of the local dataset that are contained in each minibatch of SGD. Here, c_n captures the number of required CPU cycles for device n to process one sample data, and t^{Fix} represents a fixed time duration, capturing various factors such as model training transfer between GPU and CPU. We can subsequently obtain the energy consumption of each device n during each intermediate aggregation round as

$$e_n^{\text{Cmp}} = H f_n^2 \varphi_n c_n |\mathcal{D}_n| \vartheta_n / 2, \quad (16)$$

where $\vartheta_n / 2$ represents the effective capacitance coefficient of the computing processor of device n [13].

Focusing on the model transfers between the devices and UAVs, each device n experiences two types of delays: (i) The delay when the device transmits its model to its associated UAV, which is $t_{n \rightarrow m;[g]}^{\text{D2U}} = I_n^{\text{D2U}} / r_{n \rightarrow m;[g]}^{\text{D2U}}$, where I_n^{D2U} describes the size

of local model parameters of device n . (ii) The delay when the device waits to receive the intermediate model from its associated UAV, which is $t_{m \rightarrow n;[g]}^{\text{U2D}} = I_m^{\text{U2D}} / r_{m \rightarrow n;[g]}^{\text{U2D}}$, where I_m^{U2D} represents the size of edge model parameters of UAV m . Accordingly, the overall communication delay of each device n during any of the intermediate aggregations of global round g is given by

$$t_{n;[g]}^{\text{Com}} = t_{m \rightarrow n;[g]}^{\text{U2D}} + t_{n \rightarrow m;[g]}^{\text{D2U}}. \quad (17)$$

Consequently, during each intermediate model aggregation of global round g , the overall delay, energy consumption of model transfers and energy cost at device n are given by

$$t_{n;[g]}^{\text{Dev}} = t_{n;[g]}^{\text{Cmp}} + t_{n;[g]}^{\text{Com}}, \quad (18)$$

$$e_{n;[g]}^{\text{Com}} = t_{n \rightarrow m;[g]}^{\text{D2U}} p_n^{\text{D2U}}, \quad (19)$$

$$e_{n;[g]}^{\text{Dev}} = e_n^{\text{Cmp}} + e_{n;[g]}^{\text{Com}}. \quad (20)$$

We note that to guarantee uninterrupted communication between each device n and its associated UAV during a global iteration round, it is necessary to constrain its $t_{n;[g]}^{\text{Dev}}$ to be less than the residence time within the UAV's coverage area (i.e., $t_{n;[g]}^{\text{Stay}}$), which will be enforced in our later optimization problem.

3.3.2 Energy Consumption of UAVs

When UAV m serves as an intermediate aggregator during the k^{th} intermediate aggregation of global aggregation g , its energy consumption consists of two key components: (i) *Hovering energy*, which depends on the time required for all IoT devices within the coverage of UAV m to successfully upload their local models. This duration is determined by the maximum upload time among the devices associated with UAV m during the k^{th} iteration, given by: $t_{m;[g,k]}^{\text{Hover}} = \max_{n \in \mathcal{M}_{m;[g]}^{\text{Sel}}} \{t_{n;[g]}^{\text{Dev}}\}$. (ii) *Broadcast energy*, which is influenced by the data transmission delay associated with U2D communication, denoted as $t_{m \rightarrow n;[g,k]}^{\text{U2D}}$. Subsequently, the total energy consumed by UAV m during the k^{th} intermediate aggregation of global aggregation g is given by

$$e_{m;[g,k]}^{\text{UAV}} = \underbrace{t_{m;[g,k]}^{\text{Hover}} \overline{P}_m}_{\text{hovering energy}} + \underbrace{t_{m \rightarrow n;[g,k]}^{\text{U2D}} P_m^{\text{U2D}}}_{\text{broadcast energy}}. \quad (21)$$

In our HFL architecture, UAVs have limited energy, which decreases as intermediate and global aggregations progress. This depletion may lead to potential disconnections, disrupting ongoing training. To mitigate this, we introduce energy check rules, where each UAV monitors its energy level after each round of intermediate aggregation. If a UAV meets the required energy threshold, training continues; otherwise, a global aggregation is triggered to prevent the loss of model parameters of the terrestrial IoT devices before their designated UAVs disconnect. Thus, during each global aggregation g , each active UAV can assume the following roles:

- **Role 1.** The UAV functions solely as an intermediate aggregator, responsible for intermediate aggregations.

- **Role 2.** The UAV serves both as an intermediate aggregator and the global aggregator, meaning it also performs the final aggregation at the global level.

As a result, the UAV energy consumption varies depending on the UAV's role. For example, UAVs in Role 1 do not incur the broadcasting energy costs associated with global aggregation. Additionally, if a UAV disconnects due to insufficient energy, devices within its original coverage area can no longer be associated with it, potentially impacting model convergence. To mitigate this issue and maximize resource utilization, UAV positions are dynamically adjusted in our framework, though it should be noted that UAV movement itself incurs energy costs. Consequently, to ensure a

comprehensive energy management strategy, in the following, we first model the energy consumption of UAVs throughout the training process and then define the rules governing global aggregation decisions based on UAV energy levels.

During the first k^{th} (i.e., $k \leq K_{[g]}$) rounds of intermediate iterations within the g^{th} round of global iterations, the energy loss of an active UAV m can be defined as:

$$E_{m;[g]}^{\text{UAV},k} = \sum_{k=1}^k e_{m;[g,k]}^{\text{UAV}}. \quad (22)$$

Before the start of a new global iteration round g , let the available energy of UAV m be denoted as $E_{m;[g]}^{\text{Batt}}$. To determine whether the UAV has sufficient energy to support the next round of intermediate iterations, we estimate the energy required for the upcoming $(k+1)^{\text{th}}$ intermediate iteration based on the highest energy consumption observed in previous k iterations. If the energy required for the next intermediate iteration exceeds the UAV's available energy, it indicates that the UAV will disconnect during the next round of local training. This undesired scenario can be captured by the following condition:

$$E_{m;[g]}^{\text{UAV},k} \leq E_{m;[g]}^{\text{Batt}} \leq E_{m;[g]}^{\text{UAV},k} + \max_{1 \leq k \leq k} \left\{ e_{m;[g,k]}^{\text{UAV}} \right\}. \quad (23)$$

Under this condition, the total number of intermediate iterations in the g^{th} global iteration is k . However, if a UAV has sufficient energy to continue training indefinitely, the absence of frequent global aggregations may lead to model instability and divergence due to prolonged local training without synchronization that induces model bias. To prevent this, we enforce a maximum number of edge iterations per global aggregation, denoted as K^{Max} , ensuring stability in the training process. Thus, the number of edge iterations per global iteration is given by

$$K_{[g]} = \begin{cases} k, & \phi_{[g]} = 1, \\ K^{\text{Max}}, & \phi_{[g]} = 0. \end{cases} \quad (24)$$

Here, $\phi_{[g]} = 1$ indicates that the condition in (23) holds for at least a UAV m , and thus a UAV disconnection will occur due to insufficient energy during global round g , limiting the edge iterations to k . If $\phi_{[g]} = 0$, meaning no UAV disconnections, the system enforces the maximum allowable edge iterations K^{Max} .

3.3.3 Total Energy and Delay Costs

Next, we discuss the time and energy costs of the intermediate and global aggregation processes. During the g^{th} global iteration, the time and energy costs at the local edge network rooted at UAV m (i.e., each UAV m and all its subsequent assigned devices) can be computed as follows:

$$T_{m;[g]}^{\text{Edge}} = \sum_{k=1}^{K_{[g]}} t_{m;[g,k]}^{\text{Hover}}, \quad (25)$$

$$E_{m;[g]}^{\text{Edge}} = \sum_{k=1}^{K_{[g]}} \left\{ e_{m;[g,k]}^{\text{UAV}} + \sum_{n \in \mathcal{N}_{m;[g]}^{\text{Sel}}} e_{n;[g]}^{\text{Dev}} \right\}. \quad (26)$$

Also, given the (potential) UAV relocations across two consecutive global aggregations, the total hovering energy consumption is formally defined as a function of delay and the traveling distance of each UAV m as follows:

$$E_{m;[g]}^{\text{Delay}} = T_{m;[g]}^{\text{E2G}} \overline{p}_m + \overline{p}_m^{\text{Move}} d_{m;[g]}/V_m, \quad (27)$$

$$T_{m;[g]}^{\text{Delay}} = T_{m;[g]}^{\text{E2G}} + d_{m;[g]}/V_m, \quad (28)$$

$$d_{m;[g]} = \sqrt{(\mathfrak{p}_{m;[g]}(x) - \mathfrak{p}_{m;[g-1]}(x))^2 + (\mathfrak{p}_{m;[g]}(y) - \mathfrak{p}_{m;[g-1]}(y))^2}, \quad (29)$$

where $\overline{p}_m^{\text{Move}}$ represents the average power consumption of the UAV during movement, $T_{m;[g]}^{\text{Delay}}$ represents the delay in this process, $T_{m;[g]}^{\text{E2G}} = I_m^{\text{U2U}}/r_{m \rightarrow m'}$ captures the delay of model offloading from UAV m to the global aggregator UAV m' (i.e., $X_{m';[g]} = 1$), and $d_{m;[g]}$ represents the traveling distance between the designated locations of the UAV across two consecutive global aggregations.

Once the global aggregation is completed, the global aggregator UAV (we denote it by m' for analytical simplicity) broadcasts the updated global model to all UAVs that subsequently relay it to their assigned devices, initiating the next global round. The broadcast time and energy required for this process are given by

$$T_{[g]}^{\text{Broad}} = \sum_{m' \in \mathcal{M}} X_{m';[g]} \left(\max_{m \in \mathcal{M}_{[g]} \setminus \{m'\}} \left\{ I^{\text{G}}/r_{m' \rightarrow m}^{\text{U2U}} + \max_{n \in \mathcal{N}_{m;[g]}^{\text{Sel}}} \left\{ I^{\text{G}}/r_{m' \rightarrow n}^{\text{U2D}} \right\} \right) \right), \quad (30)$$

$$E_{[g]}^{\text{Broad}} = \sum_{m' \in \mathcal{M}} X_{m';[g]} \left(\max_{m \in \mathcal{M}_{[g]} \setminus \{m'\}} \left\{ I^{\text{G}}/r_{m' \rightarrow m}^{\text{U2U}} \right\} p_{m'}^{\text{U2U}} + \sum_{m \in \mathcal{M}_{[g]}} \max_{n \in \mathcal{N}_{m;[g]}^{\text{Sel}}} \left\{ I^{\text{G}}/r_{m' \rightarrow n}^{\text{U2D}} \right\} p_m^{\text{U2D}} \right), \quad (31)$$

where I^{G} represents the size of global model. Besides, the hovering energy required by UAVs participating in the next global round is defined as

$$E_{[g]}^{\text{Bwait}} = \sum_{m \in \mathcal{M}_{[g]}} T_{[g]}^{\text{Broad}} \overline{p}_m. \quad (32)$$

Accordingly, the overall time and energy costs during the g^{th} global round can be calculated as follows:

$$T_{[g]} = T_{[g]}^{\text{Broad}} + \max_{m \in \mathcal{M}_{[g]}} \left\{ T_{m;[g]}^{\text{Edge}} + T_{m;[g]}^{\text{Delay}} \right\}, \quad (33)$$

$$E_{[g]} = E_{[g]}^{\text{Broad}} + E_{[g]}^{\text{Bwait}} + \sum_{m \in \mathcal{M}_{[g]}} \left\{ E_{m;[g]}^{\text{Edge}} + E_{m;[g]}^{\text{Delay}} \right\}. \quad (34)$$

4 PROBLEM FORMULATION

We formalize the network orchestration in our HFL scenario of interest as an optimization problem \mathcal{P}_0 , where its optimization variables include the number of local SGD iterations H , the upload bandwidth of D2U links $B_{m,n;[g]}^{\text{D2U}}$, the download bandwidth of U2D links $B_{m,n;[g]}^{\text{U2D}}$, device-to-UAV association adaptive threshold $\beta_{m;[g]}$, the location $\mathfrak{p}_{m;[g]}$ of active UAVs, and the selection of the global aggregator $X_{m;[g]}$ in each round of global iteration. This optimization problem is given by

$$\mathcal{P}_0 : \quad \underset{H, B_{m,n;[g]}^{\text{D2U}}, B_{m,n;[g]}^{\text{U2D}}, \beta_{m;[g]}, \mathfrak{p}_{m;[g]}, X_{m;[g]}}{\text{argmin}} \quad \lambda_5 E_{[g]} + \lambda_6 T_{[g]} \quad (35)$$

$$\text{s.t.} \quad 0 \leq \sum_{n \in \mathcal{N}_{m;[g]}^{\text{Sel}}} B_{m,n;[g]}^{\text{D2U}} \leq B_m^{\text{D2U}}, \quad \forall m \in \mathcal{M}_{[g]} \quad (35a)$$

$$0 \leq \sum_{n \in \mathcal{N}_{m;[g]}^{\text{Sel}}} B_{m,n;[g]}^{\text{U2D}} \leq B_m^{\text{U2D}}, \quad \forall m \in \mathcal{M}_{[g]} \quad (35b)$$

$$\mathcal{N}_{m;[g]}^{\text{Sel}} \cap \mathcal{N}_{m';[g]}^{\text{Sel}} = \emptyset, \quad \forall m, m' \in \mathcal{M}_{[g]}, m \neq m' \quad (35c)$$

$$E_{m;[g]}^{\text{UAV},k} \leq E_{m;[g]}^{\text{Batt}} \leq E_m^{\text{Batt}}, \quad \forall m \in \mathcal{M}_{[g]} \quad (35d)$$

$$\mathcal{N}_{m;[g]}^{\text{Sel}} \subset \mathcal{N}_{m;[g]}^{\text{Cov}}, \quad \forall m \in \mathcal{M}_{[g]} \quad (35e)$$

$$t_{n;[g]}^{\text{Dev}} \leq t_{n;[g]}^{\text{Stay}}, \quad \forall n \in \mathcal{N}_{m;[g]}^{\text{Sel}} \quad (35f)$$

$$\alpha_{m,n;[g]} \geq \beta_{m;[g]}, \quad \forall n \in \mathcal{N}_{m;[g]}^{\text{Sel}} \quad (35g)$$

$$H \in \mathbb{N}^+, \alpha_{m,n;[g]}, \beta_{m;[g]}, X_{m;[g]} \in [0, 1] \quad (35h)$$

$$\sum_{m \in \mathcal{M}_{[g]}} X_{m;[g]} = 1, \quad (35i)$$

where λ_5 and λ_6 represent weighting coefficients to tune the importance of time and energy cost in the objective. Also, constraints (35a) and (35b) ensures that the bandwidth allocated to devices that connect to each UAV m does not exceed the total bandwidth allocated to the UAV (denoted by B_m^{D2U} and B_m^{U2D}), constraint (35c) removes the redundancy on model transfers by ensuring that devices do not engage in simultaneous model exchanges with multiple UAVs, while constraints (35d) and (35e) ensure that the UAV's battery capacity does not exceed the initial value in each global iteration, and the devices that are selected by each UAV are among those that are covered by the UAV. Further, constraint (35f) ensures the completion of model training and transfer from each device n to its associated UAV within the dwell time of the device under the UAV's coverage. Finally, constraints (35g) and (35h) define the feasibility region of the optimization variables, while constraint (35i) enforces that, for each global aggregation round, only one UAV is selected as the global model aggregator.

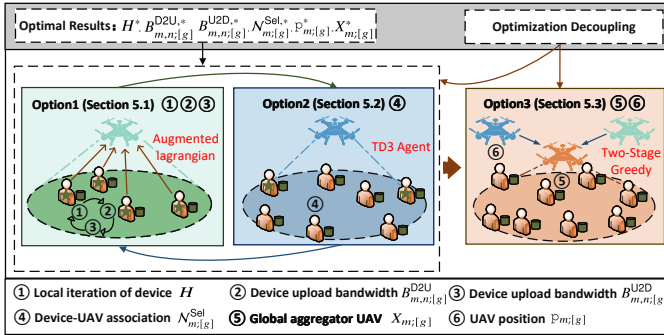


Fig. 2: An overview of our decoupling framework for solving problem \mathcal{P}_0 .

5 PROBLEM DECOMPOSITION AND SOLUTION

\mathcal{P}_0 presents a mixed-integer NP-hard optimization problem, requiring the optimization of both continuous variables, such as the bandwidth allocation $B_{m,n,[g]}^{D2U}$ and $B_{m,[g]}^{U2D}$, adaptive threshold $\beta_{m,[g]}$, and UAV positioning $\mathcal{P}_{m,[g]}$, as well as binary/discrete integer variables, such as global aggregator selection $X_{m,[g]}$ and the number of local iterations H . Further, it can be easily verified that the objective function is a non-convex function of these optimization variables, adding to the complexity of its solution design. Given such complexities, solving \mathcal{P}_0 directly is intractable.

We thus tackle \mathcal{P}_0 by decoupling it into three subproblems. The first subproblem, \mathcal{P}_1 , focuses on determining the number of local iterations H , which is relaxed and considered as a continuous variable, the bandwidth allocation $B_{m,n,[g]}^{D2U}$ for each device, and the bandwidth allocation $B_{m,[g]}^{U2D}$ for each UAV, ensuring an optimal balance between local computation and communication overhead. The second subproblem, \mathcal{P}_2 , aims to derive an adaptive device-to-UAV association strategy, optimizing the adaptive threshold $\beta_{m,[g]}$ for selecting devices that contribute most effectively to model convergence. Finally, \mathcal{P}_3 focuses on optimizing UAV positioning $\mathcal{P}_{m,[g]}$ and global aggregator selection, determining which UAV should take on the role of global aggregation by solving for $X_{m,[g]}$.

In a nutshell, the overall optimization process is divided into two sequential steps. First, \mathcal{P}_1 and \mathcal{P}_2 are iteratively optimized together, aiming to minimize local iteration costs and reduce the communication overhead between devices and UAVs. The process begins by solving \mathcal{P}_1 based on an initial device-to-UAV association, then using the resulting solution to optimize \mathcal{P}_2 . The updated device-to-UAV association is then fed back into \mathcal{P}_1 for re-evaluation, and this iterative process continues until both subproblems are adequately solved. Once \mathcal{P}_1 and \mathcal{P}_2 reach convergence,

the second step optimizes \mathcal{P}_3 based on their solutions. The UAV positions are adjusted to maximize the number of covered devices $\mathcal{N}_{m,[g]}^{\text{Cov}}$ and minimize communication costs between UAVs, ensuring efficient information exchange and stable network coverage. This structured decoupling and optimization approach allows for an efficient and scalable solution and is illustrated in Fig. 2.

5.1 Problem Formulation and Solution Design of \mathcal{P}_1

Since a single global round consists of multiple intermediate iterations, each coordinated by multiple UAVs, we define subproblem \mathcal{P}_1 as the optimization of the number of local iterations H , which is relaxed and considered to be a continuous variable, uplink bandwidth allocation $B_{m,n,[g]}^{D2U}$ and downlink bandwidth allocation $B_{m,[g]}^{U2D}$ for each UAV m and its assigned devices. The objective of \mathcal{P}_1 is to minimize the time and energy costs incurred by active each UAV (e.g., UAV m) during each intermediate aggregation. Accordingly, subproblem \mathcal{P}_1 is formulated as follows:

$$\mathcal{P}_1 : \underset{H, B_{m,n,[g]}^{D2U}, B_{m,[g]}^{U2D}}{\text{argmin}} \lambda_5 \left\{ \sum_{n \in \mathcal{N}_{m,[g]}^{\text{Sel}}} e_{n,[g]}^{\text{Dev}} + e_{m,[g,k]}^{\text{UAV}} \right\} + \lambda_6 t_{m,[g,k]}^{\text{Hover}} \quad (36)$$

s.t. (35a), (35b), (35h)

Recalling our previous discussions and (15)-(21), \mathcal{P}_1 can be further rewritten as the following optimization problem:

$$\mathcal{P}_{1a} : \underset{H, B_{m,n,[g]}^{D2U}, B_{m,[g]}^{U2D}}{\text{argmin}} \lambda_5 \left\{ \sum_{n \in \mathcal{N}_{m,[g]}^{\text{Sel}}} H f_n^2 \varphi_n c_n |\mathcal{D}_n| \theta_n / 2 + t_{n \rightarrow m,[g]}^{D2U} p_n^{D2U} + t_{m \rightarrow n,[g]}^{U2D} p_m^{U2D} + \max_{n \in \mathcal{N}_{m,[g]}^{\text{Sel}}} (t_{n,[g]}^{\text{Dev}}) \overline{p}_m \right\} + \lambda_6 \max_{n \in \mathcal{N}_{m,[g]}^{\text{Sel}}} (t_{n,[g]}^{\text{Dev}}) \quad (37)$$

s.t. (35a), (35b), (35h)

To facilitate finding the solution of \mathcal{P}_{1a} , we further introduce the following (positive) variables for notational simplicity:

$$\begin{aligned} A_n^{D2U} &= \lambda_5 I_n^{D2U} p_n^{D2U}, & \mathcal{A}_{m,n}^{D2U} &= p_n^{D2U} d_{m,n,[g]}^{-\alpha_{D2U}} / N_0, \\ A_m^{U2D} &= \lambda_5 I_m^{U2D} p_m^{U2D}, & \mathcal{A}_{m,n}^{U2D} &= p_m^{U2D} d_{m,n,[g]}^{-\alpha_{U2D}} / N_0, \\ U_{m,n}^{D2U} &= (\lambda_5 \overline{p}_m + \lambda_6) I_n^{D2U} p_n^{D2U}, & U_{m,n}^{U2D} &= (\lambda_5 \overline{p}_m + \lambda_6) I_m^{U2D} p_m^{U2D}, \\ Z_{m,n} &= (\lambda_5 \overline{p}_m + \lambda_6) \left\{ \frac{|\mathcal{D}_n| \varphi_n c_n}{f_n} + t^{\text{Fix}} \right\}, \\ C_n &= \frac{\lambda_5 f_n^2 \varphi_n c_n |\mathcal{D}_n| \theta_n}{2}. \end{aligned}$$

Accordingly, \mathcal{P}_{1a} can be further transformed into \mathcal{P}_{1b} given by (38), for which we obtain the following result.

Theorem 1. \mathcal{P}_{1b} represents a convex optimization problem.

Proof: We prove this by verifying that its first-order and second-order derivatives satisfy certain relationships in **Appendix A**.

Given the convexity of subproblem \mathcal{P}_{1b} , we adopt a penalty-based approach and transform it into an augmented Lagrangian function to facilitate optimization. This transformation allows us to effectively handle constraints while improving the stability of the solution. In particular, to determine an optimal value for the number of local iterations H , while keeping other variables (e.g., bandwidth allocation $B_{m,n,[g]}^{D2U}$, $B_{m,[g]}^{U2D}$ and adaptive threshold $\beta_{m,[g]}$) fixed, we introduce the following two constraints:

$$\mathcal{G}(H) = \max_{n \in \mathcal{N}_{m,[g]}^{\text{Sel}}} \left\{ \frac{U_n^{D2U}}{B_{m,n,[g]}^{D2U} \log_2 \left(1 + \frac{\mathcal{A}_{m,n}^{D2U}}{B_{m,n,[g]}^{D2U}} \right)} + \right.$$

$$\mathcal{P}_{1b} : \underset{H, B_{m,n;[g]}^{D2U}, B_{m,n;[g]}^{U2D}}{\operatorname{argmin}} \sum_{n \in \mathcal{N}_{m;[g]}^{\operatorname{Sel}}} \left\{ \frac{A_n^{D2U}}{B_{m,n;[g]}^{D2U} \log_2 \left(1 + \frac{\mathcal{A}_{m,n}^{D2U}}{B_{m,n;[g]}^{D2U}} \right)} + \frac{A_m^{U2D}}{B_{m,n;[g]}^{U2D} \log_2 \left(1 + \frac{\mathcal{A}_{m,n}^{U2D}}{B_{m,n;[g]}^{U2D}} \right)} + HC_n \right\} + \max_{n \in \mathcal{N}_{m;[g]}^{\operatorname{Sel}}} \left\{ \frac{U_n^{D2U}}{B_{m,n;[g]}^{D2U} \log_2 \left(1 + \frac{\mathcal{A}_{m,n}^{D2U}}{B_{m,n;[g]}^{D2U}} \right)} + \frac{U_m^{U2D}}{B_{m,n;[g]}^{U2D} \log_2 \left(1 + \frac{\mathcal{A}_{m,n}^{U2D}}{B_{m,n;[g]}^{U2D}} \right)} + HZ_{m,n} \right\}. \quad (38)$$

s.t. (35a), (35b), (35h)

$$\frac{U_m^{U2D}}{B_{m,n;[g]}^{U2D} \log_2 \left(1 + \frac{\mathcal{A}_{m,n}^{U2D}}{B_{m,n;[g]}^{U2D}} \right)} + HZ_{m,n} \Bigg\}, \quad (39)$$

$$\mathcal{Y} \geq \mathcal{G}(H), \quad (40)$$

where \mathcal{Y} indicates a slack variable. Combining (39) and (40), We rewrite the objective function of problem \mathcal{P}_{1b} as $f(H)$

$$f(H) = \sum_{n \in \mathcal{N}_{m;[g]}^{\operatorname{Sel}}} \left\{ \frac{A_n^{D2U}}{B_{m,n;[g]}^{D2U} \log_2 \left(1 + \frac{\mathcal{A}_{m,n}^{D2U}}{B_{m,n;[g]}^{D2U}} \right)} + \frac{A_m^{U2D}}{B_{m,n;[g]}^{U2D} \log_2 \left(1 + \frac{\mathcal{A}_{m,n}^{U2D}}{B_{m,n;[g]}^{U2D}} \right)} + HC_n \right\} + \mathcal{Y}. \quad (41)$$

To effectively handle the constraints in subproblem \mathcal{P}_{1b} , we introduce Lagrangian relaxation and construct an augmented Lagrangian function as follows:

$$\mathcal{L}(H, \mathcal{Y}, v) = f(H) + v(\mathcal{G}(H) - \mathcal{Y}), \quad (42)$$

where v is the Lagrange multiplier. To further improve convergence, we augment the Lagrangian function by adding a quadratic penalty term as follows:

$$\mathcal{L}_\sigma(H, \mathcal{Y}, v) = f(H) + v(\mathcal{G}(H) - \mathcal{Y}) + \frac{\sigma}{2} P(H, \mathcal{Y}), \quad (43)$$

where $P(H, \mathcal{Y}) = (\mathcal{G}(H) - \mathcal{Y})^2$ is the penalty function, and σ is the penalty factor controlling the weight of constraint violations. The optimization problem is then solved through a series of iterations, where in the j^{th} iteration (denoted by super-script $\langle j \rangle$ in the notations) the problem is formulated as:

$$\mathcal{P}_{1c} : \underset{H^{(j)}, \mathcal{Y}^{(j)}}{\operatorname{argmin}} \mathcal{L}_{\sigma^{(j)}}(H^{(j)}, \mathcal{Y}^{(j)}, v^{(j)}) \quad (44)$$

s.t. (35h), (40)

Here $v^{(j)}$ is regarded as a constant (its update will be discussed later). Since solving for both $H^{(j)}$ and $\mathcal{Y}^{(j)}$ simultaneously is challenging, we employ an iterative approach, first solving for $\mathcal{Y}^{(j)}$ and then updating $H^{(j+1)}$. In particular, given a fixed $H^{(j)}$, the subproblem related to $\mathcal{Y}^{(j)}$ can be written as

$$\mathcal{P}_{1d} : \underset{\mathcal{Y}^{(j)}}{\operatorname{argmin}} v^{(j)} (\mathcal{G}(H^{(j)}) - \mathcal{Y}^{(j)}) + \frac{\sigma^{(j)}}{2} (\mathcal{G}(H^{(j)}) - \mathcal{Y}^{(j)})^2 \quad (45)$$

s.t. (40)

For which, we obtain the following result.

Theorem 2. The value of $\mathcal{Y}^{(j)} = \max \left\{ -\frac{v^{(j)}}{\sigma^{(j)}} - \mathcal{G}(H^{(j)}), 0 \right\}$ is the optimal solution for \mathcal{P}_{1d} .

Proof: Please refer to **Appendix B**.

Substituting the above result back into $\mathcal{L}_{\sigma^{(j)}}$, we obtain

$$\mathcal{L}_{\sigma^{(j)}}(H^{(j+1)}) = f(H^{(j+1)}) + \frac{\sigma^{(j)}}{2} \mathcal{G}(H^{(j+1)})^2 - \frac{\sigma^{(j)}}{2} \left\{ \max \left\{ \frac{v^{(j)}}{\sigma^{(j)}} + \mathcal{G}(H^{(j+1)}), 0 \right\}^2 - \left(\frac{v^{(j)}}{\sigma^{(j)}} \right)^2 \right\}. \quad (46)$$

Thus, \mathcal{P}_{1c} can further be transformed into the following problem:

$$\mathcal{P}_{1e} : \underset{H^{(j+1)}}{\operatorname{argmin}} \mathcal{L}_{\sigma^{(j)}}(H^{(j+1)}) \quad (47)$$

s.t. (35h)

Since $\mathcal{Y}^{(j)}$ is eliminated, the above problem is an unconstrained optimization problem in a lower-dimensional space, enabling efficient solutions via gradient descent. Specifically, we first obtain the gradient of $H^{(j+1)}$ with respect to \mathcal{P}_{1e} according to (48) and (49)¹, and then determine whether its gradient norm $\|\nabla_{H^{(j+1)}} \mathcal{L}_{\sigma^{(j)}}(H^{(j+1)}, \mathcal{Y}^{(j)})\|_2$ meets the precision constants $\kappa^{(j)}$ to prove the optimality of the solution (i.e., $\|\nabla_{H^{(j+1)}} \mathcal{L}_{\sigma^{(j)}}(H^{(j+1)}, \mathcal{Y}^{(j)})\|_2 \leq \kappa^{(j)}$). To further ensure the adherence to constraints, we follow the three steps below to determine whether the iterations can stop or has to continue.

(I) Constraint Violation: When the precision constraint is met, we further compute the following function that characterizes the constraint violation degree of $H^{(j+1)}$:

$$\psi^{(j)}(H^{(j+1)}) = \sqrt{\max \left\{ \mathcal{G}(H^{(j+1)}), -\frac{v^{(j)}}{\sigma^{(j)}} \right\}^2}. \quad (50)$$

We then determine the relationship between the constraint violation $\varepsilon^{(j)}$ and the initial constraint violation $\varepsilon^{(0)}$ as follows.

(II) Constraint Violation is Acceptable: If the solution $H^{(j+1)}$ meets $\psi^{(j)}(H^{(j+1)}) \leq \varepsilon^{(j)}$ and $\psi^{(j)}(H^{(j+1)}) \leq \varepsilon^{(0)}$, then the algorithm terminates.

(III) Constraint Violation is Unacceptable: We consider two cases: **(Case 1)** If $H^{(j+1)}$ meets $\psi^{(j)}(H^{(j+1)}) \leq \varepsilon^{(j)}$ but $\psi^{(j)}(H^{(j+1)}) > \varepsilon^{(0)}$, we update the multiplier $v^{(j)}$ and keep the penalty factor $\sigma^{(j)}$ unchanged to approach the optimal solution. To determine how $v^{(j+1)}$ is updated, we first revisit $f(H)$ and \mathcal{P}_{1e} , and note that the optimal solution for $f(H)$, represented by H^* , \mathcal{Y}^* , and multiplier v^* , should fulfill Karush-Kuhn-Tucker (KKT) conditions. Similarly, for \mathcal{P}_{1c} , the solutions $H^{(j+1)}$ and $\mathcal{Y}^{(j+1)}$ are required to satisfy KKT conditions, as given by

$$\nabla f(H^*) + v^* \nabla \mathcal{G}(H^*) = 0, \quad (51)$$

$$\max \left\{ -\frac{v^{(j)}}{\sigma^{(j)}} - \mathcal{G}(H^{(j+1)}), 0 \right\} = \mathcal{Y}^{(j+1)}, \quad (52)$$

$$\nabla f(H^{(j+1)}) + (v^{(j)} + \sigma^{(j)} (\mathcal{G}(H^{(j+1)}) + \mathcal{Y}^{(j+1)})) \nabla \mathcal{G}(H^{(j+1)}) = 0. \quad (53)$$

Combining (51)-(53), the update rules for $v^{(j+1)}$ and $\sigma^{(j+1)}$ are

$$v^{(j+1)} = \max \left\{ v^{(j)} + \sigma^{(j)} \mathcal{G}(H^{(j+1)}), 0 \right\}, \quad (54)$$

$$\sigma^{(j+1)} = \sigma^{(j)}. \quad (55)$$

Beside, we also adjust $\kappa^{(j+1)}$ and $\varepsilon^{(j+1)}$ to better approximate the optimal solution according to Case 1 conditions below.

$$\kappa^{(j+1)} = \begin{cases} \frac{\kappa^{(j)}}{\sigma^{(j+1)}}, & \text{Case 1,} \\ \frac{1}{\sigma^{(j+1)}}, & \text{Case 2,} \end{cases}, \quad \varepsilon^{(j+1)} = \begin{cases} \frac{\varepsilon^{(j)}}{(\sigma^{(j+1)})^{-\xi_2}}, & \text{Case 1,} \\ \frac{1}{(\sigma^{(j+1)})^{-\xi_1}}, & \text{Case 2,} \end{cases}, \quad (56)$$

1. To simplify the expressions, we define $\hat{u}(H^{(j+1)}) = \frac{v^{(j)}}{\sigma^{(j)}} + \mathcal{G}(H^{(j+1)})$. In addition, $\mathbb{1}(\hat{u}(H^{(j+1)}))$ is defined as the indicator function, where $\mathbb{1}(\hat{u}(H^{(j+1)})) = 1$ if $\hat{u}(H^{(j+1)}) > 0$; otherwise, $\mathbb{1}(\hat{u}(H^{(j+1)})) = 0$.

$$\begin{aligned}
\nabla_{H^{(j+1)}} \mathcal{L}_{\sigma^{(j)}} &= \nabla f(H^{(j+1)}) + \nabla \left(\frac{\sigma^{(j)}}{2} \mathcal{G}(H^{(j+1)})^2 \right) - \nabla \left(\frac{\sigma^{(j)}}{2} \left(\max \left\{ \frac{v^{(j)}}{\sigma^{(j)}} + \mathcal{G}(H^{(j+1)}), 0 \right\} \right)^2 \right) \\
&= \nabla f(H^{(j+1)}) + \sigma^{(j)} \mathcal{G}(H^{(j+1)}) \nabla \mathcal{G}(H^{(j+1)}) + \sigma^{(j)} \cdot \max \left\{ \hat{u}(H^{(j+1)}), 0 \right\} \cdot \nabla \hat{u}(H^{(j+1)}) \cdot \mathbb{1}(\hat{u}(H^{(j+1)})) \\
&= \nabla f(H^{(j+1)}) + \sigma^{(j)} \mathcal{G}(H^{(j+1)}) Z_{m,n^*} - \sigma^{(j)} \cdot \max \left\{ \hat{u}(H^{(j+1)}), 0 \right\} Z_{m,n^*} \cdot \mathbb{1}(\hat{u}(H^{(j+1)})) \\
&= \nabla f(H^{(j+1)}) + \sigma^{(j)} \left(\mathcal{G}(H^{(j+1)}) - \max \left\{ \hat{u}(H^{(j+1)}), 0 \right\} \right) Z_{m,n^*}, \text{ (if } \mathbb{1}(\hat{u}(H^{(j+1)})) = 1)
\end{aligned} \tag{48}$$

$$H^{(j+1)} = H^{(j)} - \hat{\eta} \nabla_{H^{(j+1)}} \mathcal{L}_{\sigma^{(j)}}; Z_{m,n^*} \text{ represents the largest } Z_{m,n} \text{ in } n \in \mathcal{N}_{m,[g]}^{\text{Sel}}. \tag{49}$$

where ζ_1, ζ_2 represents two constants and $\zeta_1 \neq \zeta_2$. (**Case 2**) If $\psi^{(j)}(H^{(j+1)}) > \varepsilon^{(j)}$, we choose to keep the multiplier unchanged and update the penalty factor to better approximate the optimal solution, that is,

$$v^{(j+1)} = v^{(j)}, \tag{57}$$

$$\sigma^{(j+1)} = \rho \sigma^{(j)}, \tag{58}$$

where $\rho \in [2, 10]$ represents a fixed constant. At this time, $\kappa^{(j+1)}$ and $\varepsilon^{(j+1)}$ will also be adjusted according to Case 2 conditions in (56). Here, we obtain the following theorem to show the optimality of our proposed method.

Theorem 3. *The local minimum solution obtained by augmented Lagrangian function matches the optimal solution of the objective function $f(H)$.*

Proof: Please refer to **Appendix C**.

To obtain the solution for bandwidth allocation variables, i.e., optimizing $B_{m,n,[g]}^{\text{D2U}}$ and $B_{m,n,[g]}^{\text{U2D}}$, we need to follow the exact same procedure detailed above with H being replaced by these variables in the above formulations. Besides, we summarize our method.

Algorithm 2: Penalized Augmented Lagrangian Method for Local Iteration and Bandwidth Optimization (PALM-BLO)

- 1 **Input :** $H, v, \kappa, \varepsilon, \sigma, \zeta_1, \zeta_2, \rho, B_{m,n,[g]}^{\text{D2U}}$ and $B_{m,n,[g]}^{\text{U2D}}$;
 - 2 **Output :** $H^*, B_{m,n,[g]}^{\text{D2U,*}}$, $B_{m,n,[g]}^{\text{U2D,*}}$;
 - 3 **Initialization :** $H^{(0)}, 0 < \zeta_1 \leq \zeta_2 \leq 1, \sigma^{(0)} > 0, \kappa^{(0)} = \frac{1}{\sigma^{(0)}}$, $\varepsilon^{(0)} = \frac{1}{(\sigma^{(0)})^{-\zeta_1}}, \rho > 1$;
 - 4 **for** $j = 0, 1, \dots$ **do**
 - 5 Get $\mathcal{Y}^{(j)}$ based *Theorem 2* and $H^{(j)}$.
 - 6 Obtain the solution $H^{(j+1)}$ (based on (48), (49)) that satisfies the accuracy condition $\|\nabla_{H^{(j+1)}} \mathcal{L}_{\sigma^{(j)}}(H^{(j+1)}, \mathcal{Y}^{(j)})\|_2 \leq \kappa^{(j)}$ in \mathcal{P}_{1e} .
 - 7 **if** $\psi^{(j)}(H^{(j+1)}) \leq \varepsilon^{(j)}$ **then**
 - 8 **if** $\psi^j(H^{(j+1)}) \leq \varepsilon^{(0)}$ **then**
 - 9 Obtain approximate solution $\mathcal{Y}^{(j)}$ and $H^* \leftarrow H^{(j+1)}$, break.
 - 10 Multiplier $v^{(j+1)}$ Update based on (54).
 - 11 Penalty factor no change: $\sigma^{(j+1)} \leftarrow \sigma^{(j)}$.
 - 12 Adjust $\kappa^{(j+1)}$ and $\varepsilon^{(j+1)}$ based on (56)–case (i).
 - 13 Update penalty factor $\sigma^{(j+1)}$ based on (58), but $v^{(j+1)} \leftarrow v^{(j)}$.
 - 14 Modify $\kappa^{(j+1)}$ and $\varepsilon^{(j+1)}$ based on (56)–case (ii).
 - 15 Replace H with $B_{m,n,[g]}^{\text{D2U}}$ or $B_{m,n,[g]}^{\text{U2D}}$ and find their optimal values using the above procedure.
-

5.2 Problem Formulation and Solution Design of \mathcal{P}_2

Subproblem \mathcal{P}_2 aims to determine the device-to-UAV association during each global round, considering the mobility and heterogeneity of devices. The goal is to optimize the selection of participating devices to maximize training efficiency while ensuring reliable convergence. To achieve this, we define two key

metrics for each UAV m during the g^{th} global iteration. The first metric, $\varpi_{m,[g]}^1$ captures the difference in training loss between the previous global iteration ($g-1$) and the current iteration g , measuring the improvement in model optimization. The second metric, $\varpi_{m,[g]}^2$ evaluates the change in training accuracy, assessed using a small batch of data (by using the parameters of models such as $w_{m,[g-1,K_{[g-1]}]}^{\text{UAV}}$ and $w_{m,[g,K_{[g]}]}^{\text{UAV}}$). These metrics are formally defined as follows:

$$\varpi_{m,[g]}^1 = L(w_{m,[g-1,K_{[g-1]}]}^{\text{UAV}}) - L(w_{m,[g,K_{[g]}]}^{\text{UAV}}), \tag{59}$$

$$\varpi_{m,[g]}^2 = \text{Acc}_{m,[g,K_{[g]}} - \text{Acc}_{m,[g-1,K_{[g-1]}]}, \tag{60}$$

where $L(w_{m,[g,K_{[g]}]}^{\text{UAV}})$ and $\text{Acc}_{m,[g,K_{[g]}}$ represent the training loss and accuracy of the model of UAV m .

To balance time and energy efficiency while ensuring satisfactory training accuracy, it is important to avoid selecting devices that are either physically distant from UAVs or computationally constrained, even if their model similarity is high. Therefore, we introduce a time constraint to prevent excessive delays, ensuring that each device's training time does not exceed a predefined threshold: $t_{n,[g]}^{\text{Dev}} \leq t_n^{\text{Max}}$, where t_n^{Max} represents an acceptable deadline. The contribution of an intermediate model to the global model is then formulated as a weighted linear combination of $\varpi_{m,[g]}^1$ and $\varpi_{m,[g]}^2$, leading to the following optimization problem

$$\mathcal{P}_2 : \underset{\beta_{m,[g]}}{\text{argmax}} \quad \lambda_7 \varpi_{m,[g]}^1 + \lambda_8 \varpi_{m,[g]}^2 \tag{61}$$

$$\text{s.t.} \quad t_{n,[g]}^{\text{Dev}} \leq t_n^{\text{Max}} \tag{61a}$$

where λ_7 and λ_8 represent the weighting coefficients, $\lambda_7, \lambda_8 \in (0, 1)$ and $\lambda_7 + \lambda_8 = 1$. The values of these coefficients can be adjusted to reflect different preference settings, thereby adapting the device selection strategy based on the dataset characteristics.

Solving \mathcal{P}_2 directly is challenging due to two primary factors. First, the device-to-UAV association process is influenced by time-varying channel conditions, introducing uncertainty. These variations make it difficult to design a static optimization strategy, as the optimal selection of devices can shift dynamically due to changes in network conditions. Second, the convergence of the UAV's model in the $K_{[g]}$ -th round of aggregation, characterized by $\varpi_{m,[g]}^1$ and $\varpi_{m,[g]}^2$, depends not only on the current selection of participating devices — which is determined by the device relevance score $\alpha_{m,n,[g]}$ and the adaptive threshold $\beta_{m,[g]}$ — but also on the cumulative impact of all previous intermediate aggregations. Further, since the aggregation process builds upon prior rounds, device selection during each aggregation affects future model performance, making \mathcal{P}_2 an interdependent optimization process rather than an isolated decision at each aggregation round.

To effectively capture these dynamic dependencies, we reformulate the problem as a constrained Markov Decision Process (MDP). In this framework, state transitions are driven by the evolving performance of the UAV models and the device-to-UAV associations across multiple global rounds. By leveraging MDP-

based modeling, we enable a more adaptive and learning-driven solution, where device selection strategies can be dynamically adjusted based on both historical performance trends and real-time system conditions.

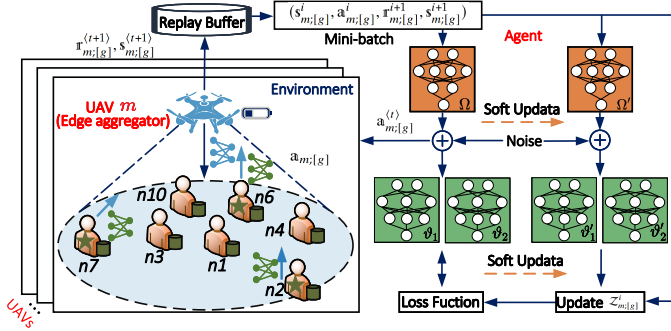


Fig. 3: A schematic of our TD3 framework.

Problem Transformation using MDP: To determine the adaptive threshold $\beta_{m:[g]}$ in each round of global iteration, we model the problem as an MDP, defined by $(\mathbf{s}, \mathbf{a}, \mathbf{r}, \gamma)$, with its elements defined as follows:

(I) **State (\mathbf{s}):** A direct indicator of UAV-aggregated edge model performance is its prediction accuracy and training loss evaluated on mini-batch datasets of global test data. Therefore, the state for UAV m , which is later fed to the TD3 agent, is defined as: $\mathbf{s}_{m:[g]} = [L(w_{m:[g],K_{[g]}^{UAV}}), Acc_{m:[g],K_{[g]}}]$.

(II) **Action (\mathbf{a}):** Once the state is observed, the TD3 agent aims to change the state of MDP via determining the adaptive threshold, which dictates the selection of devices for model training. The action is thus defined as: $\mathbf{a}_{m:[g]} = [\beta_{m:[g]}]$.

(III) **Reward (\mathbf{r}):** The reward function evaluates the contribution of selected devices to global model convergence based on the UAV-aggregated model's performance. It quantifies the improvement in loss and accuracy, guiding the TD3 agent toward better exploration and is defined as

$$\mathbf{r}_{m:[g]}(\mathbf{s}, \mathbf{a}) = \lambda_7 \varpi_{m:[g]}^1 + \lambda_8 \varpi_{m:[g]}^2. \quad (62)$$

MDP-Based Optimization of Device Selection: To maximize the cumulative reward across global iterations, we reformulate \mathcal{P}_2 as the following constrained MDP problem:

$$\mathcal{P}_{2a} : \operatorname{argmax}_{\{\beta_{m:[g]}\}_{g=1}^G} \sum_{g=1}^G \gamma^{g-1} \mathbf{r}_{m:[g]}(\mathbf{s}, \mathbf{a}) \quad (63)$$

s.t. (61a),

where γ^{g-1} is the discount factor ensuring long-term reward maximization and G represents the number of global iterations required to reach (11). Note that the actions and states of \mathcal{P}_{2a} are in high-dimensional space and the environment has certain dynamics, which is difficult to solve directly. To address this challenge, we introduce a penalty term in the reward function, transforming the problem into the following form:

$$\mathcal{P}_{2b} : \operatorname{argmax}_{\{\beta_{m:[g]}\}_{g=1}^G} \sum_{g=1}^G \gamma^{g-1} \{ \mathbf{r}_{m:[g]}(\mathbf{s}, \mathbf{a}) - \tilde{\alpha}(g) \tilde{\mathcal{Y}}_{m:[g]} \} \quad (64)$$

s.t. $\tilde{\mathcal{G}}_{m:[g]}(\mathbf{s}) \leq 0, \forall g$

where $\tilde{\mathcal{Y}}_{m:[g]} = \max(\tilde{\mathcal{G}}_{m:[g]}(\mathbf{s}), 0)^2$ represents the penalty term accounts for constraint violations. Specifically, we have $\tilde{\mathcal{G}}_{m:[g]}(\mathbf{s}) = r_{n:[g]}^{\text{Dev}} - r_n^{\text{Max}}$, and $\tilde{\alpha}(g)$ denotes the penalty coefficient during the g^{th} global iteration. Regarding the optimality of this transformation, we obtain the following theorem:

Theorem 4. When $\tilde{\alpha}(g)$ is sufficiently large, the solution of \mathcal{P}_{2b} approximates that of \mathcal{P}_{2a} , thereby effectively managing the trade-off between constraint satisfaction and reward maximization.

Proof: Please refer to **Appendix D**.

TD3-Based Adaptive Threshold Determination: TD3 is an off-policy reinforcement learning (RL) algorithm that extends Deep Deterministic Policy Gradient (DDPG) to improve stability and performance in continuous action spaces. Unlike standard RL approaches, TD3 mitigates overestimation bias, which is common in value-based RL algorithms that rely on Q-learning updates [34], [35]. Overestimation occurs when the action-value function (Q-function) systematically overestimates the expected return, leading to suboptimal policy updates. This issue is especially problematic in continuous control tasks, such as optimizing \mathcal{P}_{2b} , where precise selection of the adaptive threshold $\beta_{m:[g]}$ is required. TD3 effectively addresses these challenges through three key improvements over DDPG: (i) **Clipped Double Q-Learning:** TD3 employs two Q-value networks and updates only the minimum Q-value estimate to avoid overestimation bias, ensuring that the learned policy does not exploit inaccurate Q-value estimations. (ii) **Delayed Policy Updates:** The policy network (actor) is updated less frequently than the Q-value networks, preventing the policy from being trained on rapidly fluctuating or inaccurate value estimates. (iii) **Target Policy Smoothing:** To improve exploration robustness, TD3 adds noise to the target action before computing the target Q-value, making the policy more resistant to local perturbations and leading to better generalization in dynamic environments. These improvements make TD3 particularly well-suited for optimizing \mathcal{P}_{2b} , where the adaptive threshold $\beta_{m:[g]}$ must be carefully adjusted over multiple iterations in response to changing system conditions.

To tackle \mathcal{P}_{2b} , we deploy a TD3-based agent at each UAV. In particular, each TD3 agent uses a deep neural network to learn the approximate action value function $Q_{\vartheta}(\mathbf{s}_{m:[g]}, \mathbf{a}_{m:[g]})$ and the deterministic policy $\mu_{\Omega}(\mathbf{s}_{m:[g]})$, where ϑ and Ω represent the parameters of the value network and the policy network. Specifically, for each TD3 agent, there are four value networks (2 predictive value networks $Q_{\vartheta_1}, Q_{\vartheta_2}$ and 2 target value networks $Q_{\vartheta'_1}, Q_{\vartheta'_2}$) and two policy networks (predictive policy network μ_{Ω} , target policy network $\mu_{\Omega'}$). Each TD3 agent follows a deep neural network setup tailored to the state and action space of \mathcal{P}_{2b} : the value network consists of an input layer, two hidden layers, and an output layer. The input layer takes two state variables $\mathbf{s}_{m:[g]}$ (training loss and accuracy) and one action variable $\mathbf{a}_{m:[g]}$ (adaptive threshold). The output layer produces the Q-value. Also, the actor network follows a similar structure to the value network but outputs a continuous action instead of a Q-value.

At each global iteration g , the TD3 agent at each UAV m follows seven steps:

(I) **Action Selection:** For each time step $t \in \{1, 2, \dots, t^{\text{Step}}\}$, the agent generates an action based on the deterministic policy and exploration noise:

$$\mathbf{a}_{m:[g]}^{(t)} = \mu_{\Omega}(\mathbf{s}_{m:[g]}^{(t)}) + \tilde{\epsilon}, \quad (65)$$

where $\tilde{\epsilon} \sim \text{clip}(\tilde{N}(0, \tilde{\sigma}), -\tilde{c}, \tilde{c})$ is Gaussian exploration noise, and \tilde{c} represents the amplitude limit of the added noise. The optimal threshold $\beta_{m:[g]}^*$ is selected based on the action that maximizes the cumulative reward.

(II) **Reward Computation:** After executing the selected action $\mathbf{a}_{m:[g]}$, the TD3 agent computes the reward:

$$\mathbf{r}_{m:[g]}^{(t+1)} = \mathbf{r}_{m:[g]}^{(t+1)}(\mathbf{s}^{(t)}, \mathbf{a}^{(t)}) - \tilde{\alpha}(g) \tilde{\mathcal{Y}}_{m:[g]}^{(t+1)}, \quad (66)$$

where $\tilde{\mathcal{Y}}_{m;[g]}^{(t+1)}$ is a penalty term for constraint violations.

(III) Experience Replay: The agent stores each transition experience $(s_{m;[g]}^{(t)}, a_{m;[g]}^{(t)}, r_{m;[g]}^{(t)}, s_{m;[g]}^{(t+1)})$ in an experience replay buffer \mathcal{B} with a maximum capacity $|\mathcal{B}|_{\max}$.

(IV) Value Network Update: The TD3 agent samples a mini-batch B from \mathcal{B} (i.e., $B \subset \mathcal{B}$) and computes the updated action using the target policy network:

$$a_{m;[g]}^{i+1,t'} = \mu_{\Omega'}(s_{m;[g]}^{i+1,t'}) + \tilde{\varepsilon}^i, \tilde{\varepsilon}^i \sim \text{clip}(\tilde{N}(0, \tilde{\sigma}), -\tilde{c}, \tilde{c}), \quad (67)$$

where $i = \{1, 2, \dots, |B|\}$ is defined as the i^{th} sample. The target Q-value is then computed as:

$$\mathcal{Z}_{m;[g]}^i = r_{m;[g]}^{i+1,t'} + \gamma^{g-1} \min_{j=1,2} Q_{\vartheta'_j}(s_{m;[g]}^{i+1,t'}, a_{m;[g]}^{i+1,t'}), \quad (68)$$

where j represents the j^{th} Q-value networks. Finally, the value network parameters ϑ are updated using Mini-Batch Gradient Descent (MBGD) with the gradient

$$\nabla_{\vartheta} L(\vartheta) \approx \frac{1}{|B|} \sum_{i=1}^{|B|} (\mathcal{Z}_{m;[g]}^i - Q(s_{m;[g]}^i, a_{m;[g]}^i)) \nabla_{\vartheta} Q(s_{m;[g]}^i, a_{m;[g]}^i). \quad (69)$$

(V) Policy Network Update: After every d updates of the value network, the policy network parameters Ω are updated using Mini-Batch Gradient Ascent (MBGA) with the gradient

$$\nabla_{\Omega} J(\Omega) \approx \frac{1}{|B|} \sum_{i=1}^{|B|} \nabla_{\Omega} \mu_{\Omega}(s_{m;[g]}^i) \nabla_{a^i} Q_{\Omega}(s_{m;[g]}^i, a_{m;[g]}^i). \quad (70)$$

(VI) Penalty Coefficient Update: The penalty coefficient is updated incrementally as follows:

$$\tilde{\alpha}(g+1) = \begin{cases} \tilde{\alpha}(g) + \Delta \tilde{\alpha}, & \text{if } t \bmod d = 0, \\ \tilde{\alpha}(g), & \text{otherwise,} \end{cases} \quad (71)$$

where $\Delta \tilde{\alpha}$ represents a constant used to gradually increase the penalty coefficient.

(VII) Target Network Soft Update: The value and policy networks are soft-updated as follows:

$$\begin{cases} \vartheta' \leftarrow \tau \vartheta + (1 - \tau) \vartheta', \\ \Omega' \leftarrow \tau \Omega + (1 - \tau) \Omega', \end{cases} \quad (72)$$

where $\tau \in (0, 1)$ is the update coefficient. Based on the TD3 agent, we select appropriate thresholds $\beta_{m;[g]}$ for selecting devices in each round of global iterations for each UAV. The full algorithmic process of our method is outlined in Alg. 3.

5.3 Problem Formulation and Solution Design of \mathcal{P}_3

After at least one UAV disconnects, the device coverage of the remaining UAVs decreases, leading to two significant challenges. First, the model trained by the disconnected UAV cannot be aggregated in time, causing slower convergence of the global model and increasing the overall training cost. Second, with fewer UAVs available, fewer devices participate in training, further reducing learning efficiency. To mitigate these issues, we propose a proactive UAV selection and redeployment strategy. Specifically, before a UAV disconnects, an appropriate global aggregation UAV is selected to collect and aggregate models from all active UAVs, ensuring uninterrupted model training. Simultaneously, UAVs are redeployed to maximize device coverage, keeping as many devices as possible engaged in subsequent intermediate and global aggregation rounds. However, optimizing UAV repositioning and aggregator selection presents additional challenges. In particular, the movement of UAVs to new locations results in variable mobility energy consumption, directly impacting system efficiency. Additionally, the uplink energy required to transmit models to

Algorithm 3: Multi-Criteria Device-to-UAV Associations with Adaptive Threshold (MCCUA-AT)

```

1 Input :  $\gamma, \tau, d, \lambda_1, \lambda_2, \lambda_3, v_m^{\text{Per}}, \mathcal{N}_{m;[g]}^{\text{Cov}}$ ;
2 Output:  $\mathcal{N}_{m;[g]}^{\text{Sel}}$ ;
3 Initialization :  $Q_{\vartheta_1}, Q_{\vartheta_2}, Q_{\vartheta'_1}, Q_{\vartheta'_2}, \mu_{\Omega}, \mu_{\Omega'}, \beta_{m;[g]}$ ,
 $\mathcal{N}_{m;[g]}^{\text{Sel}} = \emptyset$ ;
4 if the global model parameter changes does not satisfy (11) then
5   for each UAV  $m \in \mathcal{M}_{[g]}$  do
6     for time step  $t = \{1, 2, \dots, t^{\text{Step}}\}$  do
7       TD3 process: // running at online UAV
8         1. Execute actions to update rewards and status:  $r_{m;[g]}^{(t+1)}$ ,
 $s_{m;[g]}^{(t+1)}$  based on (65), (66).
9         2. Store experience:  $(s_{m;[g]}^{(t)}, a_{m;[g]}^{(t)}, r_{m;[g]}^{(t)}, s_{m;[g]}^{(t+1)})$ 
into  $\mathcal{B}$ .
10        3. Select a small batch of  $B$  experience transfer
samples: (i) Calculate  $a_{m;[g]}^{i+1,t'}$  based on (67) and (ii)
update  $\mathcal{Z}_{m;[g]}^i$  based on (68).
11        4. Use MBGD update value network parameter  $\vartheta$ 
based on (69).
12        if  $t \bmod d$  then
13          Use MBGA update policy network parameter  $\Omega$ 
based on (70).
14          Update penalty coefficient based on (71).
15          Soft update  $\vartheta'$  and  $\Omega'$  based on (72).
16        5. Select the action with the largest reward in the time step
as the output  $a_{m;[g]}$ .
17        Device-UAV Association: //running at online UAV
18        for  $n \in \mathcal{N}_{m;[g]}^{\text{Cov}}$  do
19          6. UAV broadcasts  $v_m^{\text{Per}}$ , which devices use to calculate
 $R_{m,n;[g]}, d_{m,n;[g]}, f_n$ .
20          7. All devices transmit  $R_{m,n;[g]}, d_{m,n;[g]}, f_n$  to the
corresponding UAV, which will be used to calculate
 $S_{m,n;[g]}^{\text{Sim}}, S_{m,n;[g]}^{\text{Dis}}, S_{m,n;[g]}^{\text{Fre}}$ .
21          8. Calculate  $\alpha_{m,n;[g]}$  according to (13).
22          9. Get  $\beta_{m;[g]}: \beta_{m;[g]} \leftarrow a_{m;[g]}$ .
23          if  $\alpha_{m,n;[g]} \geq \beta_{m;[g]}$  then
24            Choose device  $n$  and set  $\mathcal{N}_{m;[g]}^{\text{Sel}} \leftarrow \{n\}$ .
25        if device  $n$  in multiple UAVs coverage areas then
26          Device  $n$  will be associated with a UAV with the highest
 $\alpha_{m,n;[g]}$ .

```

the global aggregation UAV and the broadcast energy required to distribute the updated model depend on the location of the selected global aggregator. Therefore, finding the optimal UAV positions and aggregator selection strategy is crucial to minimizing overall system costs while ensuring robust learning performance. Based on these considerations, we obtain an optimization problem to jointly determine the optimal UAV repositioning strategy, ensuring maximum device coverage while minimizing mobility energy consumption, and the selection of the global aggregation UAV, reducing both uplink transmission energy for edge models and the broadcast energy of the global model. The formal optimization formulation is presented as follows:

$$\mathcal{P}_3: \underset{\mathcal{P}_{m;[g]}, X_{m;[g]}}{\text{argmin}} \lambda_5 \left\{ E_{[g]}^{\text{Broad}} + E_{[g]}^{\text{Bwait}} + \sum_{m \in \mathcal{M}_{[g]}} E_{m;[g]}^{\text{Delay}} \right\} + \lambda_6 \left\{ T_{[g]}^{\text{Broad}} + \max_{m \in \mathcal{M}_{[g]}} T_{m;[g]}^{\text{Delay}} \right\} \quad (73)$$

$$\text{s.t. (35d), (35e), (35h), (35i)}$$

Solving this problem directly is computationally challenging due to the interdependencies between UAV repositioning and

global aggregator selection. To address this, we decompose the problem into a two-stage optimization framework. Specifically, the first stage optimizes the position of the UAV in the g^{th} global iteration (i.e., $\mathcal{P}_{m;[g]}$), and the second stage optimizes the selection of the central aggregator UAV, which determining m for $X_{m;[g]} = 1$. Next we will describe this process in detail.

Algorithm 4: Two-Stage Greedy for UAV Redeployment and Central Aggregator Selection (TSG-URCAS)

```

1 Input :  $\mathcal{P}_{m;[g]}$ ,  $\mathcal{M}_{[g]}$ ,  $V_m$ ,  $\overline{p}_m^{\text{Move}}$ ,  $\chi_1$ ,  $\chi_2$ ;
2 Output :  $X_{m;[g]} = 1$ ,  $\mathcal{P}_{m;[g]}$ ;
3 Initialization :  $\mathcal{V}_{m;[g]}^{(0,0)}$ ,  $\overline{\mathcal{V}}_{m;[g]}^{(0)}$ ,  $\overline{\mathcal{V}}_{m;[g]}^* = +\infty$ ,  $\hat{b} = 0$ ,  $d_m^{\text{Set}} = 0$ ;
4 for each UAV server  $m \in \mathcal{M}_{[g]}$  do
5   Stage 1: // Rough Search
6   if  $q \leq \chi_1$  then
7     for  $\hat{a} = \{1, 2, \dots, 10\}$  do
8       Calculate UAV coverage  $|\mathcal{N}_{m;[g]}^{\text{Cov}}|^{(\hat{a}, \hat{b})} / |\mathcal{N}_{m;[g]}^{\text{Cov}}|^{(\hat{b}-1)}$ .
9       Obtain  $\mathcal{V}_{m;[g]}^{(\hat{a}, \hat{b})}$  based on (74).
10      if  $\mathcal{V}_{m;[g]}^{(\hat{a}, \hat{b})} > \mathcal{V}_{m;[g]}^{(\hat{b})}$  then
11         $\mathcal{V}_{m;[g]}^{(\hat{b})} \leftarrow \mathcal{V}_{m;[g]}^{(\hat{a}, \hat{b})}$ 
12      if  $\mathcal{V}_{m;[g]}^{(\hat{b})} < \tilde{\xi}_1$  then
13         $q += 1$ 
14      Update the UAV  $m$ 's position.
15     $\hat{b} += 1$ 
16   $\hat{b} = 0$ .
17  Stage 1: // Precise Search
18  Same as the rough search steps, but explore directions from 10
  to 20, and  $\chi_1 \rightarrow \chi_2$ .
19 Stage 2: // global aggregator UAV choose
20 for  $m \in \mathcal{M}_{[g]}$  do
21   Calculate distance between UAV  $m$  and remaining online UAVs
   $d_{m' \rightarrow m;[g]}^{\text{UAV}}$  and sum of all online UAV-to-UAV distances and
  obtain  $\overline{\mathcal{V}}_{m;[g]}$  based on (75).
22   if  $\overline{\mathcal{V}}_{m;[g]} \leq \overline{\mathcal{V}}_{m;[g]}^*$  then
23      $\overline{\mathcal{V}}_{m;[g]}^* \leftarrow \overline{\mathcal{V}}_{m;[g]}$ .
24 Select the UAV corresponding to  $\overline{\mathcal{V}}_{m;[g]}^*$  and set  $X_{m;[g]} = 1$ .

```

(I) First Stage: We determine the UAV's moving direction through *rough search* and *precise search*. In the rough search stage, the UAV moves a fixed distance in 10 different directions and evaluates the change in device coverage after each move, using it as a reward metric. The UAV selects the direction that maximizes device coverage. However, since excessive movement may lead to high energy consumption, we define a benefit function to balance coverage expansion and movement cost. Specifically, the benefit of moving to the \hat{a} -th direction for the \hat{b} -th attempt during the rough search in the g^{th} global round is defined as follows:

$$\mathcal{V}_{m;[g]}^{(\hat{a}, \hat{b})} = \lambda_9 \left\{ \frac{|\mathcal{N}_{m;[g]}^{\text{Cov}}|^{(\hat{a}, \hat{b})}}{|\mathcal{N}_{m;[g]}^{\text{Cov}}|^{(\hat{b}-1)}} - 1 \right\} - \lambda_{10} \left\{ \frac{\hat{b} d_m^{\text{Set}}}{V_m \overline{p}_m^{\text{Move}}} \right\}, \quad (74)$$

where $\frac{|\mathcal{N}_{m;[g]}^{\text{Cov}}|^{(\hat{a}, \hat{b})}}{|\mathcal{N}_{m;[g]}^{\text{Cov}}|^{(\hat{b}-1)}} - 1$ represents the relative increase in device coverage, $\frac{\hat{b} d_m^{\text{Set}}}{V_m \overline{p}_m^{\text{Move}}}$ represents the cumulative energy consumption due to UAV movement and d_m^{Set} represents the distance moved of a single rough search. The UAV moves in the direction with the highest benefit value $\mathcal{V}_{m;[g]}^{(\hat{b})}$. If the maximum benefit does not exceed a predefined threshold $\tilde{\xi}_1$ for χ_1 consecutive iterations, the UAV enters the precise search stage (at this time, \hat{b} will be reset to 0 for the next calculation). In this stage, the UAV explores 15

finer movement directions within a smaller radius and re-evaluates the comprehensive benefit. If no movement direction achieves a benefit higher than $\tilde{\xi}_2$ for χ_2 consecutive iterations, the UAV is considered to have reached its optimal position.

(II) Second Stage: Once UAV repositioning is finalized, we determine the global aggregation UAV based on a communication cost function, which accounts for the distance between the UAV selected as the central aggregator and the other UAVs. In particular, the benefit function for selecting UAV m as the central aggregator for the $(g+1)^{\text{th}}$ global iteration is defined as follows:

$$\overline{\mathcal{V}}_{m;[g]} = \sum_{\forall m' \in \mathcal{M}, m' \neq m} d_{m' \rightarrow m;[g]}^{\text{UAV}}, \quad (75)$$

where $d_{m' \rightarrow m;[g]}^{\text{UAV}}$ represents the distance between UAV m' to m . We naturally select the UAV with the smallest $\overline{\mathcal{V}}_{m;[g]}$ (i.e., $\overline{\mathcal{V}}_{m;[g]}^*$), that is, the sum of the distances from the selected central aggregator to the remaining UAVs) as global aggregator (i.e. $X_{m;[g]} = 1$). The detailed UAV repositioning and aggregator selection process is outlined in Alg. 4.

6 EVALUATIONS

In the following, we conduct experiments to evaluate the performance of our proposed approach, abbreviated as ‘‘CEHFed’’ for brevity, standing for ‘‘Cost Effective Hierarchical Federated Learning’’. To ensure a comprehensive evaluation, we adopt a dual-perspective analysis. First, we benchmark CEHFed against state-of-the-art HFL methods, utilizing standard evaluation metrics such as test accuracy, training time, and energy efficiency (see Section 6.3.1). Second, recognizing the unique challenges addressed in this work — UAV dropouts during training and dynamic device mobility across UAV coverage areas — we conduct scenario-based evaluations that specifically assess CEHFed's performance in such dynamic environments (see Section 6.3.2).

6.1 Network and Machine Learning Settings

Our experiments are conducted in a 20 km \times 20 km area, where 5 UAVs provide coverage for 150 terrestrial IoT devices. Each UAV has a coverage radius of 5 km, enabling dynamic interactions between devices and UAVs as they move within the network. We consider that in each global iteration, each device will leave the coverage area of its associated UAV with probability ξ , the default value of which is chosen to be 0.3.

- **Dataset and training models:** We use both the MNIST and Fashion-MNIST (FaMNIST) datasets, which are widely used for classification tasks. MNIST consists of handwritten digits (0-9) across 10 categories, while FaMNIST contains 10 categories of grayscale clothing images, each with a resolution of 28 \times 28 pixels. To evaluate model performance, we employ three different neural network architectures: CNN, LeNet-5, and VGG, with corresponding parameter sizes of 21,840, 206,922, and 60,074, respectively [14], [40], [41]. These datasets and models allow us to assess CEHFed's efficiency across varying computational complexities and dataset characteristics.

- **Data heterogeneity:** For MNIST and FaMNIST, we examine two distinct non-i.i.d. data distribution scenarios. In the first case, referred to as non-iid (A), each device holds data samples from only two labels, creating a highly non-iid data distribution. In the second case, non-iid (B), each device contains data from at least two labels (the number of labels of each device is chosen uniformly at random between two and ten), while maintaining the same total

number of data samples as in the first case, leading to a slightly more balanced distribution.

- *Resource heterogeneity*: The heterogeneity of device resources is primarily reflected in differences in computing capabilities, such as varying CPU frequency speeds. The detailed specifications of computing resources, along with other key system settings, are provided in Table 1.

TABLE 1: Simulation Setting

Parameter	Value
\mathcal{H}	UAV height: 150 m
ϑ_n	Chipset capacitance coefficient: 10^{-28}
c_n	Number of CPU cycles: [30,100] cycle/bit
f_n	IoT devices' CPU frequencies: [1,10] GHz
N_0	Power spectral density of AWGN: -174 dBm/Hz
$\overline{p_m}$	UAV's hovering powers: 100 W
p_n^{D2U}	IoT devices' transmit powers: [200,800] mW
p_m^{U2U}	UAVs' transmit powers: [500,1000] mW
p_m^{U2D}	UAVs' broadcast powers: [300,1200] mW
B_m^{D2U}, B_m^{U2D}	Total bandwidth resource of UAV m : [20,100] MHz
K^{Max}	Maximum number of edge iterations: 10
$\eta, \hat{\eta}$	Learning rate: 0.001, 0.002
χ_1, χ_2	Maximum consecutive rough and precise searches allowed: 8, 6.

6.2 Benchmark Methods

We compare our approach against several benchmark methods described below, representing different strategies in FL and HFL.

- *CFed*: A conventional FL mechanism, where a certain number of devices are efficiently selected for each global iteration [36].
- *HFed*: An HFL mechanism that aims to optimize device selection during each edge iteration only, without optimizing the number of local training and bandwidth allocation (use our solution of \mathcal{P}_2) [37].
- *RHFed*: An HFL mechanism that randomly selects devices while optimizing the number of local training and bandwidth allocation (use our solution of \mathcal{P}_1).
- *GDHFed*: An HFL mechanism that selects devices based on their proximity to UAVs (i.e., only $S_{m,n;[g]}^{Dis}$ is considered while calculating $\alpha_{m,n;[g]}$), while optimizing the number of local training and bandwidth allocation (use our solution of \mathcal{P}_1).
- *GSHFed*: An HFL mechanism that selects devices with model difference score with UAVs (i.e., only $S_{m,n;[g]}^{Sim}$ is considered while calculating $\alpha_{m,n;[g]}$), while optimizing the number of local training and bandwidth allocation (use our solution of \mathcal{P}_1).
- *AHFed*: Adds an adversarial training part to conventional HFL to reduce the negative impact of device data heterogeneity [38].
- *HFedAT*: An HFL mechanism that combines synchronous inner-layer training and asynchronous cross-layer training, without considering data heterogeneity of devices [39].

6.3 Performance Comparisons

We begin by comparing performance using standard evaluation metrics, including test accuracy, training time, and energy efficiency (Section 6.3.1). Since our work addresses unique challenges, such as UAV dropouts during the training process, we further conduct scenario-based simulations to demonstrate the adaptability of our proposed framework, highlighting its advantages in dynamic UAV-assisted HFL environments (Section 6.3.2).

6.3.1 Experiments with conventional evaluating metrics

Convergence Performance: We begin by evaluating the convergence performance across different learning models and datasets, as illustrated in Fig. 4. Examining the results holistically, we observe that CEHFed's convergence performance is either comparable to or outperforms the benchmark methods, with only marginal performance trade-offs in certain cases. However, these plots alone do not provide insight into the key performance metrics of interest, such as energy consumption and latency. More critically, it is essential to assess whether CEHFed's comparable or superior convergence is achieved with significantly lower network resource consumption in terms of energy and delay. The short answer is yes — our approach achieves this performance while maintaining notably lower resource overhead. To substantiate this, in the following, we first examine training delay and then analyze energy consumption to demonstrate the efficiency of CEHFed in UAV-assisted HFL.

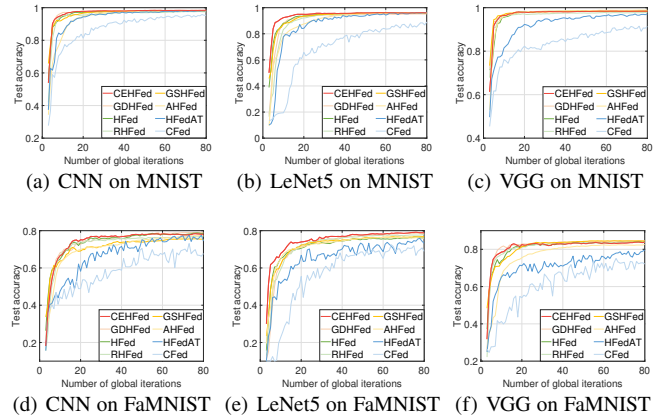


Fig. 4: Performance comparisons in terms of test accuracy on MNIST and FaMNIST datasets using different models.

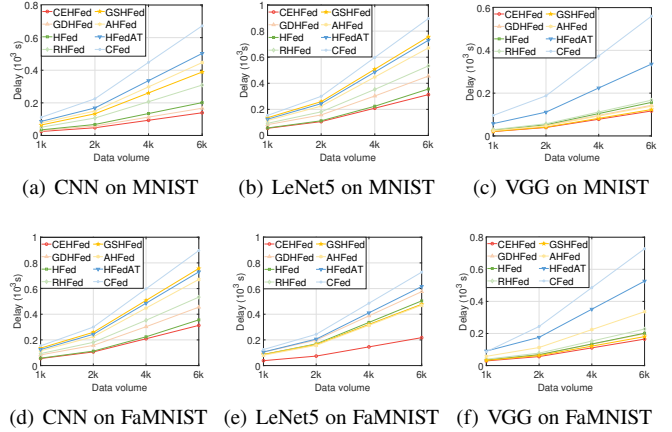


Fig. 5: Time cost of model training on MNIST and FaMNIST datasets upon having different models.

Time Cost (Delay) Performance: We next analyze the time cost incurred by different methods during the HFL process, evaluating performance across varying data volumes². As shown in Fig. 5, our proposed CEHFed consistently outperforms all benchmark methods in terms of time efficiency. This improvement is attributed to our well-optimized bandwidth allocation and adaptive device selection strategy, which significantly reduces edge iteration time. Furthermore, our dynamic selection of the global aggregator

² Data volumes refers to the number of data points used for training during the model training process.

ensures minimal data loss and reduces communication delays between edge and global aggregators. For instance, in Fig. 5(a), when training CNN on MNIST, CEHFed achieves a time cost reduction of 17%, 63%, and 55% compared to GDHFed, GSHFed, and RHFed, respectively, when processing a 4k data volume. The primary reason for this improvement is that benchmark methods relying on random or greedy-based device selection often fail to adaptively choose devices that best suit the training process, leading to inefficiencies in iteration scheduling. Additionally, compared to HFed, CEHFed reduces overall training time by 31% for the same data volume. When compared to CFed, AHFed, and HFedAT, CEHFed achieves an even more significant time reduction of 79%, 69%, and 73%, respectively. These results underscore the superior efficiency of our framework, demonstrating its ability to accelerate HFL training while optimizing resource utilization in UAV-assisted networks.

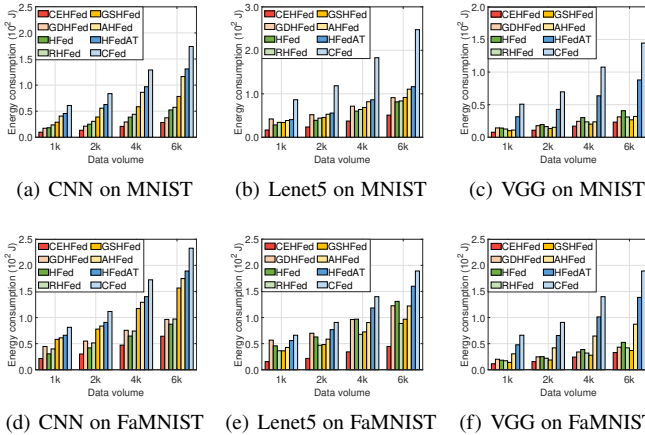


Fig. 6: Energy consumption of the model training operations on MNIST and FaMNIST datasets upon having different models.

Energy Consumption Performance: We next analyze the overall energy consumption throughout the HFL process, as shown in Fig. 6. It is important to note that energy cost does not directly correlate with time cost — a lower training time does not necessarily imply lower energy consumption. For example, when comparing GDHFed and RHFed on CNN and FaMNIST (depicted in Fig. 5(d) and Fig. 6(d)), RHFed incurs a higher time cost than GDHFed, yet its energy consumption is comparable to or even lower than GDHFed. This discrepancy arises because time and energy costs are not linearly related, as discussed in Section 3.3. From Fig. 6, it is evident that CEHFed significantly outperforms all benchmark methods in energy efficiency. Specifically, our approach reduces overall energy consumption by 62%, 52%, and 47% compared to GDHFed, GSHFed, and RHFed, respectively. The primary reason is that GDHFed accounts only for communication costs while neglecting computation overhead, whereas GSHFed considers some computation costs but overlooks communication energy consumption. RHFed, on the other hand, fails to account for either factor, leading to inefficient energy utilization. Further, CEHFed achieves a 64% energy cost reduction compared to HFed. When compared to CFed, AHFed, and HFedAT, our method further reduces energy consumption by 75%, 61.8%, and 70.8%, respectively. These improvements underscore the effectiveness of CEHFed’s joint optimization strategy, which balances communication, computation, and training efficiency, leading to significant energy savings in UAV-assisted HFL.

Given that our study focuses on UAV-assisted HFL scenarios, where UAVs may drop out due to energy constraints and devices

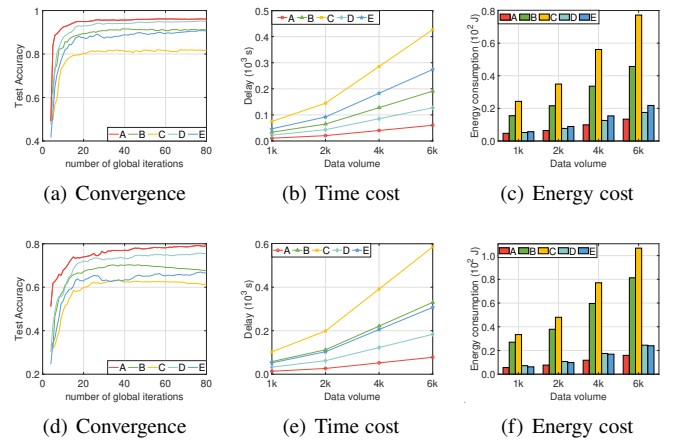


Fig. 7: Performance Comparisons upon having either adaptive and fixed thresholds. ‘A’ represents the Adaptive Threshold, while ‘B’, ‘C’, ‘D’, and ‘E’ correspond to fixed thresholds set at 0.40, 0.55, 0.70, and 0.85, respectively. The comparison is conducted using the LeNet-5 model on the MNIST (top row plots) and FaMNIST datasets (bottom row plots).

with non-i.i.d. data dynamically move across different UAVs, this section presents simulations to assess CEHFed’s performance under various configurations of such factors.

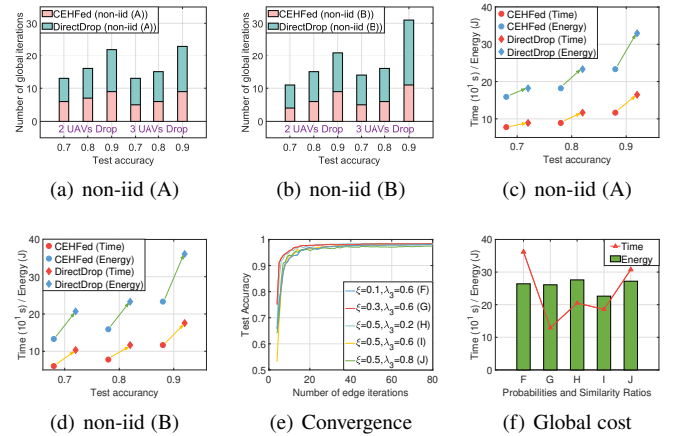


Fig. 8: (a), (b), (c), (d): Performance comparison in terms of the required number of edge iterations, time, and energy consumption to reach various test accuracies under different data distributions. (e): The impact of different mobility patterns and the coefficient of data distribution in fitness score on model convergence. (f) The impact of different mobility patterns and the coefficient of data distribution in fitness score (the letters ‘F’, ‘G’, ‘H’, ‘I’, and ‘J’ are specified in the legend of plot (e)) on energy and time costs.

Impact of Adaptive vs. Fixed Thresholds on Convergence and Resource Utilization: In Fig. 7, we evaluate the impact of adaptive thresholding compared to fixed thresholds in UAV-assisted HFL using LeNet-5 on MNIST (top row plots) and FaMNIST (bottom row plots). Our results indicate that CEHFed with adaptive thresholding achieves faster convergence than its variations with fixed thresholds. This improvement stems from the fact that excessively high thresholds limit device participation, slowing convergence, while low thresholds allow remote or less-capable devices to participate, reducing training efficiency.

For instance, when training LeNet-5 on MNIST with a 4k data volume (Figs. 7(b)), the adaptive threshold (‘A’) reduces time costs by 68.4%, 85.9%, 52.7%, and 78% compared to ‘B’, ‘C’, ‘D’, and ‘E’, respectively. Likewise, energy costs (Figs. 7(c)) decrease by 70.6%, 82.6%, 23.6%, and 38.5%, respectively. This demonstrates that an appropriate, UAV-specific threshold accelerates global model convergence and improves resource efficiency. The same

trend is observed for LeNet-5 on FaMNIST (Figs. 7(d)-(f)), revealing the effectiveness of CEHFed’s adaptive thresholding strategy.

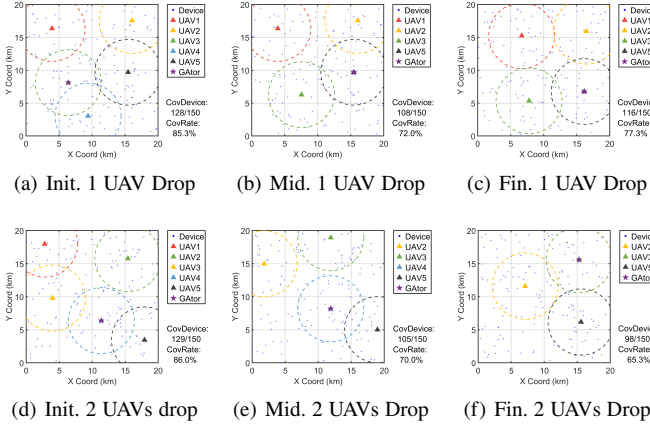


Fig. 9: Redeployment dynamics of UAVs following disconnection events.

Resilience Against UAV Dropouts: Impact on Edge Iterations and Convergence:

In Fig. 8, we examine the effect of UAV dropouts on convergence performance by comparing CEHFed with DirectDrop, a benchmark method that assumes direct UAV disconnections without mitigation strategies. We simulate scenarios where 2 or 3 out of 5 UAVs drop out, under varying data distributions. As expected, achieving higher test accuracy requires more edge iterations, increasing UAV flight duration. In Fig. 8(a), for the non-iid (A) scenario (where devices hold data from only two labels), CEHFed effectively mitigates data loss, maintaining a lower number of required edge iterations. The same holds for non-iid (B), where devices contain more than two labels. Further, Figs. 8(a) and 8(b) reveal that UAV disconnections have a greater impact as the number of labels per device increases. Specifically, under non-iid (B), achieving the same accuracy requires 6 to 12 additional edge iterations compared to non-iid (A). This suggests that greater data heterogeneity amplifies the impact of UAV dropouts, making them more disruptive to global model convergence.

Reduction in Time and Energy Costs: In Figs. 8(c) and 8(d), we analyze the time and energy costs needed to reach accuracy levels of 0.7, 0.8, and 0.9 for CEHFed vs. DirectDrop. For a 6k data volume, CEHFed reduces time and energy costs by 29.2% and 29% for non-iid (A), and 33.6% and 35.37% for non-iid (B), respectively. These results validate CEHFed’s ability to sustain efficient training even under UAV disconnections, demonstrating its superior resource utilization.

Impact of Device Mobility and Data Distribution on Convergence: In Fig. 8(e), we analyze how device mobility (ξ) and the coefficient of influence of data distribution difference score λ_1 impact model convergence. Our results reveal that the convergence performance of $\xi = 0.3$ and $\lambda_1 = 0.6$ aligns with that of $\xi = 0.5$ and $\lambda_1 = 0.2$, while the convergence of $\xi = 0.5$ and $\lambda_1 = 0.6$ aligns with that of $\xi = 0.5$ and $\lambda_1 = 0.8$. Interestingly, the overall convergence rate of the former cases is slightly higher than the latter, suggesting that at the same mobility probability, a higher coefficient of influence of data distribution difference score can reduce convergence speed. This implies that the optimal value of λ_1 is dynamic and varies with different mobility conditions, an area that warrants further investigation and we leave as future work. Additionally, comparing different mobility settings with the same λ_1 shows that an increase in device speed generally leads to faster convergence due to better data mixing across UAVs (e.g., $\xi = 0.1$, $\lambda_1 = 0.6$ vs. $\xi = 0.3$, $\lambda_1 = 0.6$), reducing the

impact of non-i.i.d. data on the model’s performance. However, when device mobility is excessively high ($\xi = 0.5$), convergence speed no longer improves due to frequent model reassignments disrupting effective training. In Fig. 8(f), we evaluate the global cost under different mobility probabilities (ξ) and data distribution influence coefficients (λ_1). We observe that as mobility increases (comparing ‘F’ vs ‘G’, ‘G’ vs ‘I’), time cost initially decreases but then rises again, whereas energy consumption consistently decreases. Additionally, selecting an appropriate coefficient of influence of data distribution difference score can further optimize both time and energy costs (comparing ‘H’ vs ‘I’ vs ‘J’), although further exploration is needed to determine the optimal balance.

UAV Redeployment Performance After Disconnections: In Fig. 9, we present the performance of the two-stage greedy algorithm proposed in this work, evaluating its effectiveness when one or two UAVs disconnect and require redeployment. Fig. 9(a) illustrates the initial scenario, where UAV 4 disconnects at a specific round of global iterations. Following this, Figs. 9(b) and 9(c) depict the network state after UAV 4’s disconnection and the subsequent redeployment of the remaining UAVs. During this process, the UAV coverage rate for devices initially drops from 85% to 72% but recovers to 77.3% after redeployment, demonstrating the algorithm’s ability to restore network coverage efficiently. Figs. 9(d)-(f) further examine the scenario where both UAV 1 and UAV 4 disconnect. When UAV 1 is lost, the coverage rate decreases by 16%, followed by an additional 4.7% drop when UAV 4 disconnects.

TABLE 2: Device coverage analysis for various UAV redeployment methods.

	1 UAV drop (%)					2 UAVs drop (%)		
	1	2	3	4	5	1 and 2	1 and 4	3 and 5
\underline{L}	-8.21	4.67	-8.67	-8.00	-6.32	-14.66	-16.00	-11.33
						-7.34	-4.70	-8.67
\underline{M}	-17.34	-21.33	-24.05	-23.34	-21.06	-23.34	-20.13	-16.22
						-7.66	-24.07	-19.33
\underline{N}	-9.67	-9.34	-1.33	-6.67	-8.67	-11.81	-12.67	-8.67
						-12.00	-13.50	-16.20

TABLE 3: Energy consumption of various UAV redeployment methods.

	1 UAV drop (J)					2 UAVs drop (J)		
	1	2	3	4	5	1 and 2	1 and 4	3 and 5
\underline{L}	20.62	22.97	21.56	18.00	20.10	10.78	9.84	10.75
						31.87	25.63	15.62
\underline{N}	48.48	53.36	42.03	33.06	39.43	45.42	58.86	30.29
						74.27	66.55	46.40

For better comparison, we designed two methods: (*M-i*) After the UAV is disconnected, the UAV does not move (i.e., the UAV is directly dropped). (*M-ii*) Constructed by integrating UAV energy consumption, coverage rate, and inter-UAV communication energy, the benefit function is optimized using a greedy algorithm to identify the solution that maximizes its value during the movement process, and the letters ‘L’ corresponds to our method, ‘M’ corresponds to (*M-i*), and ‘N’ corresponds to (*M-ii*). In Table 2, we compare the changes in UAV coverage rate of the three methods when a UAV is dropped (e.g., in our method, while UAV 1 is disconnected, causing the overall UAV coverage rate to drop by 8.21%), and when 2 UAVs are dropped (e.g., in our method, the coverage rate drops by 14.66% after UAV 1 is dropped, and then the coverage rate drops by an additional 7.34% after UAV 2 is dropped). We can also find that, if no UAV repositioning

occurs, the coverage reduction is more severe, dropping by 20.13% and 24.07% for UAV 1 and UAV 4, respectively (see Table 2, M). These results confirm that our proposed redeployment strategy effectively mitigates device coverage loss caused by UAV disconnections. Additionally, for the disconnection event in the same scenario, we compare the energy consumed by the UAV in our method and ‘N’ — which is the best baseline according to Table 2 — in the process of finding the optimal position in Table 3. These results further demonstrate that our proposed algorithm achieves a lower UAV redeployment energy costs compared to the best baseline. Collectively, the results in Tables 2 and 3 unveil that our method strikes a desirable balance between maintaining UAV coverage and minimizing UAV mobility energy costs.

7 CONCLUSION AND FUTURE WORK

In this paper, we explored a UAV-assisted HFL architecture over dynamic IoT devices, where the training process is affected by the energy limitations of UAVs. We provided a framework to optimize the learning configuration, bandwidth allocation, device-to-UAV association, global aggregator selection, and UAV redeployment strategies so as to minimize global training costs while maintaining a high model accuracy. Through extensive simulations using real-world datasets, we demonstrated that our approach reduces global training time and energy consumption, while also mitigating the negative impact of UAV disconnections on model convergence. For future research, one promising direction is the integration of satellite communication into UAV-assisted HFL, enabling seamless global model aggregation and enhancing connectivity in remote or infrastructure-limited environments. Satellites can serve as high-altitude aggregators, assisting UAVs in maintaining continuous learning even during UAV disconnections or redeployments. Another potential direction is the utilization of energy-harvesting UAVs, which can prolong operational time and reduce reliance on external charging infrastructure. By leveraging solar, wind, or RF energy harvesting, UAVs can potentially sustain FL tasks longer, improving network and learning resilience.

REFERENCES

- [1] Q. Li et al., “A Survey on Federated Learning Systems: Vision, Hype and Reality for Data Privacy and Protection”, *IEEE Trans. Knowl. Data Eng.*, vol. 35, no. 4, pp. 3347-3366, April. 2023.
- [2] B. Xie et al., “MOB-FL: Mobility-Aware Federated Learning for Intelligent Connected Vehicles”, *IEEE Int. Conf. Commun. (ICC)*, Rome, Italy, 2023, pp. 3951-3957.
- [3] W. Wu, M. Li et al., “Split Learning over Wireless Networks: Parallel Design and Resource Management”, *IEEE J. Sel. Areas Commun.*, vol. 41, no. 4, pp. 1051-1066, April. 2023.
- [4] Y. Zhang et al., “FedMDS: An Efficient Model Discrepancy-Aware Semi-Asynchronous Clustered Federated Learning Framework”, *IEEE Trans. Parallel Distrib. Syst.*, vol. 34, no. 3, pp. 1007-1019, March. 2023.
- [5] W. Sun, Y. Zhao, W. Ma et al., “Accelerating Convergence of Federated Learning in MEC With Dynamic Community”, *IEEE Trans. Mobile Comput.*, vol. 23, no. 2, pp. 1769-1784, Feb. 2024.
- [6] S. Sun et al., “Staleness-Controlled Asynchronous Federated Learning: Accuracy and Efficiency Tradeoff”, *IEEE Trans. Mobile Comput.*, vol. 23, no. 12, pp. 12621-12634, Dec. 2024.
- [7] K. -H. Chang, T. -C. Chiu and J. -P. Sheu, “VISIT: Virtual-Targeted Sequential Training with Hierarchical Federated Learning on Non-IID Data”, *IEEE Int. Conf. Commun. (ICC)*, Denver, CO, USA, 2024, pp. 5455-5460.
- [8] C. Feng, H. H. Yang et al., “Mobility-Aware Cluster Federated Learning in Hierarchical Wireless Networks”, *IEEE Trans. Wireless Commun.*, vol. 21, no. 10, pp. 8441-8458, Oct. 2022.
- [9] B. Wu et al., “Client Selection and Cost-Efficient Joint Optimization for NOMA-Enabled Hierarchical Federated Learning”, *IEEE Trans. Wireless Commun.*, vol. 23, no. 10, pp. 14289-14303, Oct. 2024.
- [10] Z. Qu, R. Duan, L. Chen et al., “Context-Aware Online Client Selection for Hierarchical Federated Learning”, *IEEE Trans. Parallel Distrib. Syst.*, vol. 33, no. 12, pp. 4353-4367, Dec. 2022.
- [11] Q. Wu et al., “HiFlash: Communication-Efficient Hierarchical Federated Learning With Adaptive Staleness Control and Heterogeneity-Aware Client-Edge Association”, *IEEE Trans. Parallel Distrib. Syst.*, vol. 34, no. 5, pp. 1560-1579, May. 2023.
- [12] Y. Ren, C. Wu and D. K. C. So, “Joint Edge Association and Aggregation Frequency for Energy-Efficient Hierarchical Federated Learning by Deep Reinforcement Learning”, *IEEE Int. Conf. Commun. (ICC)*, Rome, Italy, 2023, pp. 3639-3645.
- [13] S. Luo, X. Chen, Q. Wu et al., “HFEL: Joint Edge Association and Resource Allocation for Cost-Efficient Hierarchical Federated Edge Learning”, *IEEE Trans. Wireless Commun.*, vol. 19, no. 10, pp. 6535-6548, Oct. 2020.
- [14] J. Xu, H. Fan, Q. Wang et al., “Adaptive Idle Model Fusion in Hierarchical Federated Learning for Unbalanced Edge Regions”, *IEEE Trans. Netw. Sci. Eng.*, vol. 11, no. 5, pp. 4603-4616, Sept.-Oct. 2024.
- [15] M. Ye et al., “Heterogeneous Federated Learning: State-of-the-art and Research Challenges”, *ACM Comput. Surv.*, vol. 56, no. 3, pp. 0360-0300, May. 2023.
- [16] H. Yang et al., “Privacy-Preserving Federated Learning for UAV-Enabled Networks: Learning-Based Joint Scheduling and Resource Management”, *IEEE J. Sel. Areas Commun.*, vol. 39, no. 10, pp. 3144-3159, Oct. 2021.
- [17] C. Huang et al., “Fair Resource Allocation for Hierarchical Federated Edge Learning in Space-Air-Ground Integrated Networks via Deep Reinforcement Learning With Hybrid Control”, *IEEE J. Sel. Areas Commun.*, vol. 42, no. 12, pp. 3618-3631, Dec. 2024.
- [18] L. Zou et al., “When Hierarchical Federated Learning Meets Stochastic Game: Toward an Intelligent UAV Charging in Urban Prosumers”, *IEEE Internet Things J.*, vol. 10, no. 12, pp. 10438-10461, Dec. 2023.
- [19] J. Xu et al., “Federated Learning Powered Semantic Communication for UAV Swarm Cooperation”, *IEEE Trans. Wireless Commun.*, vol. 31, no. 4, pp. 140-146, Aug. 2024.
- [20] Ruslan et al., “UAV-assisted Unbiased Hierarchical Federated Learning: Performance and Convergence Analysis”, *arXiv preprint*, arXiv: 2407.07739, 2024.
- [21] X. Song et al., “Multitask and Multiobjective Joint Resource Optimization for UAV-Assisted Air-Ground Integrated Networks Under Emergency Scenarios”, *IEEE Internet Things J.*, vol. 10, no. 23, pp. 20342-20357, Dec. 2023.
- [22] C. Liu, T. J. Chua and J. Zhao, “Time Minimization in Hierarchical Federated Learning,” *IEEE/ACM Symp. Edge Comput. (SEC)*, Seattle, WA, USA, 2022, pp. 96-106.
- [23] T. Qi et al., “Hwamei: A Learning-Based Synchronization Scheme for Hierarchical Federated Learning”, *Int. Conf. Distrib. Comput. Syst. (ICDCS)*, Hong Kong, 2023, pp. 534-544.
- [24] Y. Li, X. Qin, H. Chen et al., “Energy-Aware Edge Association for Cluster-Based Personalized Federated Learning,” *IEEE Trans. Veh. Technol.*, vol. 71, no. 6, pp. 6756-6761, June. 2022.
- [25] Z. Dong, X. Zhu, J. Cao et al., “Fuzzy Logic Assisted Client Selection and Energy-Efficient Joint Optimization for Hierarchical Federated Learning”, *IEEE Int. Conf. Commun. (ICC)*, Rome, Italy, 2023, pp. 1262-1267.
- [26] Z. Tong et al., “Blockchain-Based Trustworthy and Efficient Hierarchical Federated Learning for UAV-Enabled IoT Networks”, *IEEE Internet Things J.*, vol. 11, no. 21, pp. 34270-34282, Oct. 2024.
- [27] R. Khelf, E. Driouch and W. Ajib, “On the Optimization of UAV-Assisted Wireless Networks for Hierarchical Federated Learning,” *IEEE Annual Int. Symp. Personal, Indoor and Mobile Radio Commun. (PIMRC)*, Toronto, ON, Canada, 2023, pp. 1-6.
- [28] H. Li and J. Huang, “Hierarchical Federated Deep Reinforcement Learning Based Joint Communication and Computation for UAV Situation Awareness”, *Elsevier Veh. Commun.*, vol. 50, pp. 100853, Dec. 2024.
- [29] J. Tang et al., “Multi-UAV-Assisted Federated Learning for Energy-Aware Distributed Edge Training”, *IEEE Trans. Netw. Serv. Manag.*, vol. 21, no. 1, pp. 280-294, Feb. 2024.
- [30] S. Wang et al., “UAV-Assisted Online Machine Learning Over Multi-Tiered Networks: A Hierarchical Nested Personalized Federated Learning Approach”, *IEEE Trans. Netw. Serv. Manage.*, vol. 20, no. 2, pp. 1847-1865, Oct. 2023.
- [31] C. Feng et al., “Mobility-Aware Cluster Federated Learning in Hierarchical Wireless Networks”, *IEEE Trans. Wireless Commun.*, vol. 21, no. 10, pp. 8441-8458, Oct. 2022.
- [32] C. Tang et al., “Mobility Accelerates Learning: Convergence Analysis on Hierarchical Federated Learning in Vehicular Networks”, *IEEE Trans. Veh. Technol.*, vol. 74, no. 1, pp. 1657-1673, Jan. 2025.

- [33] Y. Zhao et al., "Federated Learning with Non-IID Data", *arXiv preprint*, arXiv: 1806.00582., 2018.
- [34] F. G. Wakgra, W. Yahya et al., "Ratio-Based Offloading Optimization for Edge and Vehicular-Fog Federated Systems: A Multi-Agent TD3 Approach", *IEEE Trans. Veh. Technol.*, vol. 73, no. 11, pp. 17684-17696, Nov. 2024.
- [35] Z. Liang et al., "TD3-Based Collaborative Computation Offloading and Charging Scheduling in Multi-UAV-Assisted MEC Networks", *IEEE Wireless Commun. Net. Conf. (WCNC)*, Dubai, Apr. 2024, pp. 1-6.
- [36] S. Wang et al., "Performance Optimization for Variable Bitwidth Federated Learning in Wireless Networks", *IEEE Trans. Wireless Commun.*, vol. 23, no. 3, pp. 2340-2356, Mar. 2024.
- [37] R. Ha et al., "Optimal Resource Management for Hierarchical Federated Learning Over HetNets With Wireless Energy Transfer", *IEEE Internet Things J.*, vol. 10, no. 19, pp. 16945-16958, May. 2023.
- [38] X. Fang et al., "Robust Asymmetric Heterogeneous Federated Learning With Corrupted Clients", *IEEE Trans. Pattern Anal. Mach. Intell.*, vol. 47, no. 4, pp. 2693-2705, Jan. 2025.
- [39] Z. Chai et al., "FedAT: A Communication-Efficient Federated Learning Method with Asynchronous Tiers Under Non-IID Data", *IEEE Trans. Inter. Conf. High Perf. Comp. Netw. Sto. Analy.*, USA, 2021, pp. 1-17.
- [40] V. Ashu et al., "Cellular Automaton With CNN", *arXiv preprint*, arXiv: 2503.02652., 2025.
- [41] C. Sestito et al., "3D-TrIM: A Memory-Efficient Spatial Computing Architecture for Convolution Workloads", *arXiv preprint*, arXiv: 2502.18983., 2025.
- [42] Y. Dai et al., "The Rate of Convergence of Augmented Lagrangian Method for Minimax Optimization Problems with Equality Constraints", *Journal of the Opera. Resear. Soc. of China.*, vol. 12, no. 2, pp. 256-297, Jun. 2024.

APPENDIX A

Proof of Theorem 1: Convex functions have the following properties:

- **Additivity property :** If f_1, f_2, \dots, f_I is a convex function, then their linear combination (i.e., weighted sum) is also a convex function.
- **Maximum property :** If f_1, f_2, \dots, f_I is a convex function, then their pointwise maximum $\text{Max}(f_1, f_2, \dots, f_I)$ is also a convex function.

Combined with (38), we only need to prove that the following function is a convex function

$$f(H, B_{m,n;[g]}^{\text{D2U}}, B_{m,n;[g]}^{\text{U2D}}) = \underbrace{HC_n}_{\textcircled{1}} + \underbrace{\frac{A_n^{\text{D2U}}}{B_{m,n;[g]}^{\text{D2U}} \log_2(1 + \frac{A_n^{\text{D2U}}}{B_{m,n;[g]}^{\text{D2U}})}}_{\textcircled{2}} + \underbrace{\frac{A_m^{\text{U2D}}}{B_{m,n;[g]}^{\text{U2D}} \log_2(1 + \frac{A_m^{\text{U2D}}}{B_{m,n;[g]}^{\text{U2D}})}}_{\textcircled{3}}. \quad (76)$$

Since H and C_n are positive values, $\textcircled{1}$ is a convex function, and the expressions of $\textcircled{2}$ and $\textcircled{3}$ are similar, so we show the convexity of $\textcircled{2}$ using a similar approach to which the convexity of $\textcircled{3}$ can be proved. We choose $B_{m,n;[g]}^{\text{D2U}}$ from (76) as the variable x , build a new function $f(x)$, and show its convexity in the following. Firstly, we set $c_1 = A_n^{\text{D2U}}$, and $c_2 = A_m^{\text{U2D}}$ to simplify the calculation. Then, we calculate the first-order derivative of $\textcircled{2}$ as follows:

$$\begin{aligned} f(x) &= \frac{c_1}{x \log_2(1 + \frac{c_2}{x})} = \frac{c_1 \ln 2}{x \ln(1 + \frac{c_2}{x})}, \quad (77) \\ f'(x) &= \frac{(c_1 \ln 2)' x \ln(1 + \frac{c_2}{x}) - (c_1 \ln 2)(x \ln(1 + \frac{c_2}{x}))'}{(x \ln(1 + \frac{c_2}{x}))^2} \\ &= -\frac{(c_1 \ln 2)(x \ln(1 + \frac{c_2}{x}))'}{(x \ln(1 + \frac{c_2}{x}))^2} \\ &= -\frac{(c_1 \ln 2)(\ln(1 + \frac{c_2}{x}) - \frac{c_2}{x+c_2})}{(x \ln(1 + \frac{c_2}{x}))^2}. \quad (78) \end{aligned}$$

While $x > 0$, $f'(x)$ is always less than 0, so $f(x)$ is monotonically decreasing. Next, we set $\mathbf{g}(x) = \ln(1 + \frac{c_2}{x})$ and $\mathbf{h}(x) = \frac{c_2}{x+c_2}$, and obtain the second-order derivative of $\textcircled{2}$ as follows

$$\begin{aligned} f''(x) &= -\frac{(c_1 \ln 2)(\mathbf{g}(x) - \mathbf{h}(x))}{(x\mathbf{g}(x))^2} \\ &= \frac{d}{dx} \frac{-(c_1 \ln 2)(\mathbf{g}(x) - \mathbf{h}(x))}{(x\mathbf{g}(x))^2} \\ &= \frac{u'v - uv'}{v^2}, \quad (79) \end{aligned}$$

where $u = (c_1 \ln 2)(\mathbf{g}(x) - \mathbf{h}(x))$, $v = (x\mathbf{g}(x))^2$, and their corresponding derivatives are given by

$$\begin{cases} u' = \frac{d}{dx}(u) - c_1 \ln 2 \cdot (\mathbf{g}'(x) - \mathbf{h}'(x)), \\ v' = \frac{d}{dx}(v) = 2(x\mathbf{g}(x))(\mathbf{g}(x) + x\mathbf{g}'(x)), \\ \mathbf{g}'(x) = -\frac{c_2}{x^2+c_2x}, \mathbf{h}'(x) = -\frac{c_2}{(x+c_2)^2}. \end{cases} \quad (80)$$

Thus, we can get

$$\begin{aligned} f''(x) &= \frac{-c_1 \ln 2 \cdot (\mathbf{g}'(x) - \mathbf{h}'(x))}{(x\mathbf{g}(x))^2} + \\ &\quad \frac{2c_1 \ln 2 \cdot (\mathbf{g}(x) - \mathbf{h}(x))(\mathbf{g}(x) + x\mathbf{g}'(x))}{(x\mathbf{g}(x))^3}. \quad (81) \end{aligned}$$

Replacing x back with $B_{m,n;[g]}^{\text{D2U}}$, noting that $B_{m,n;[g]}^{\text{D2U}} \geq 0$ (based on (35a)), $f''(B_{m,n;[g]}^{\text{D2U}})$ is always greater than 0, so $\textcircled{2}$ is a convex function. Similarly, we can also prove that $\textcircled{3}$ is a convex function, and combined with the properties of convex functions, we can prove that \mathcal{P}_{2b} is a convex problem.

APPENDIX B

Proof of Theorem 2: To determine the optimal value of the variable $\mathcal{Y}^{(j)}$ while keeping the variable $H^{(j)}$ fixed, we take the derivative of the function with respect to $\mathcal{Y}^{(j)}$ and identify its critical points. Specifically, we have

$$\frac{df(\mathcal{Y}^{(j)})}{d\mathcal{Y}^{(j)}} = v^{(j)} + \sigma^{(j)} \left\{ \mathcal{G}(H^{(j)}) - \mathcal{Y}^{(j)} \right\}. \quad (82)$$

Setting the above derivative to 0, we get

$$\begin{cases} v^{(j)} + \sigma^{(j)} \left\{ \mathcal{G}(H^{(j)}) - \mathcal{Y}^{(j)} \right\} = 0, \\ \mathcal{Y}^* = -\frac{v^{(j)}}{\sigma^{(j)}} - \mathcal{G}(H^{(j)}). \end{cases} \quad (83)$$

From the above, the corresponding critical point $\mathcal{Y}^* = -\frac{v^{(j)}}{\sigma^{(j)}} - \mathcal{G}(H^{(j)})$ can be obtained, which, however, may be unable to satisfy the non-negative constraint, namely, $\mathcal{Y}^{(j)} \geq 0$. Accordingly, we consider the following two cases:

- If $\mathcal{Y}^* \geq 0$, meaning that $-\frac{v^{(j)}}{\sigma^{(j)}} - \mathcal{G}(H^{(j)}) \geq 0$. Then, at the point $\mathcal{Y}^{(j)} = \mathcal{Y}^*$, we get the optimal solution.
- If $\mathcal{Y}^* < 0$, the optimal solution for $\mathcal{Y}^{(j)}$ is 0 because $\mathcal{Y}^{(j)}$ can not be negative.

The above discussions imply the proof of *Theorem 2*.

APPENDIX C

Proof of Theorem 3: Proving the convergence of the augmented Lagrangian function is based on the following foundations:

- Objective function $f(H)$ and the constraint function $\mathcal{G}(H)$ are continuously differentiable.
- The problem has a feasible solution and satisfies constraint normative conditions (e.g., linear independence constraint norm (LICQ)).
- The augmented Lagrangian function can find the global minimum in each iteration.

Revisiting Appendix A, we can see that $f(H)$ and $\mathcal{G}(H)$ are continuously differentiable, and $f(H)$ is a convex function, so the augmented Lagrangian function can find the global minimum in each iteration. Besides, $\nabla \mathcal{G}(H)$ is always less than 0, which means that at the feasible point H^* , $\nabla \mathcal{G}(H^*) \neq 0$ always holds. Now that the above foundations are verified, we turn into proving the convergence of the augmented Lagrangian function, which requires verification of four conditions [42]:

(I) Monotonicity: We use the gradient descent method and update the Lagrange multiplier to approach the minimum value $H^{(j)}$ and $\mathcal{Y}^{(j)}$. Also, through Appendix B and (48), (49), it can be obtained that the value of the augmented Lagrangian function decreases monotonically during the iteration process, that is, it satisfies:

$$\mathcal{L}_{\sigma^{(j)}}(H^{(j+1)}, \mathcal{Y}^{(j+1)}, v^{(j+1)}) \leq \mathcal{L}_{\sigma^{(j)}}(H^{(j)}, \mathcal{Y}^{(j)}, v^{(j)}), \quad (84)$$

(II) Boundedness: From **(I)**, since the value of the augmented Lagrangian function is monotonically decreasing, and $f(H)$ and $\mathcal{G}(H)$ are continuous, we can naturally deduct the boundedness of $H^{(j)}$, $\mathcal{Y}^{(j)}$ and $v^{(j)}$.

(III) Limit point satisfies the KKT conditions: To verify that any limit point $H^{(j)}$, $\mathcal{Y}^{(j)}$, $v^{(j)}$ satisfies the KKT conditions, it is necessary to satisfy both the gradient condition and the feasibility condition, which are defined as

$$\begin{cases} \nabla f(H^*) + v^* \nabla \mathcal{G}(H^*) = 0, \\ \mathcal{G}(H^*) = \mathcal{Y}^*. \end{cases} \quad (85)$$

Since for $H^{(j+1)}$, $\mathcal{Y}^{(j+1)}$ is the minimum value of $\mathcal{L}_{\sigma^{(j)}}$, we can obtain that

$$\nabla f(H^{(j+1)}) + (v^{(j)} + \sigma^{(j)}(\mathcal{G}(H^{(j+1)}) + \mathcal{Y}^{(j+1)})) \nabla \mathcal{G}(H^{(j+1)}) = 0. \quad (86)$$

Besides, while $j \rightarrow +\infty$, we get that $\mathcal{G}(H^{(j+1)}) - \mathcal{Y}^{(j+1)} \rightarrow 0$. Thus, the KKT conditions are satisfied.

(IV) Convergence speed: Under appropriate conditions (e.g., $\sigma^{(j+1)}$ is large enough), the augmented Lagrangian method has a linear convergence rate, which is because the Hessian of the augmented Lagrangian is positive definite near the solution and the increase of $\sigma^{(j+1)}$ accelerates the decay of the optimality gap/error.

The above discussions prove the convergence of the augmented Lagrangian algorithm with penalty term.

APPENDIX D

Proof of Theorem 4: The optimal policy of \mathcal{P}_{2a} denoted by π^* , is the one that maximizes the cumulative reward:

$$\pi^* = \arg \max_{\pi} \mathbb{E} \left[\sum_{g=1}^G \gamma^{g-1} \mathbf{r}_{m;[g]}(\mathbf{s}, \mathbf{a}) \mid \pi \right]. \quad (87)$$

In the set of policies that satisfy constraint $\tilde{G}_{m;[g]}(\mathbf{s}) \leq 0$, we have the optimal cumulative reward $\bar{\mathbf{r}}^*$ for \mathcal{P}_{2a} , defined as

$$\bar{\mathbf{r}}^* = \arg \max_{\pi} \mathbb{E} \left[\sum_{g=1}^G \gamma^{g-1} \mathbf{r}_{m;[g]}(\mathbf{s}, \mathbf{a}) \mid \tilde{G}_{m;[g]}(\mathbf{s}) \leq 0, \forall g \right]. \quad (88)$$

Upon having penalty terms, the optimal strategy $\tilde{\pi}$ maximizes cumulative reward for \mathcal{P}_{2b} :

$$\tilde{\pi} = \arg \max_{\pi} \mathbb{E} \left[\sum_{g=1}^G \gamma^{g-1} \{ \mathbf{r}_{m;[g]}(\mathbf{s}, \mathbf{a}) - \tilde{\alpha}(g) \tilde{\mathcal{Y}}_{m;[g]} \} \mid \pi \right]. \quad (89)$$

Next, we show our analysis from three aspects: *(i) Behavior analysis of the penalty term:* For any state that violates the constraint (i.e., $\tilde{G}_{m;[g]}(\mathbf{s}) > 0$), the penalty term is:

$$\tilde{\alpha}(g) \cdot \max(\tilde{G}_{m;[g]}(\mathbf{s}), 0)^2 = \tilde{\alpha}(g) \cdot \tilde{G}_{m;[g]}(\mathbf{s})^2. \quad (90)$$

As $\tilde{\alpha}(g) \rightarrow \infty$, the penalty term tends towards infinity. Thus, when choosing the optimal strategy, it will strongly suppress the strategies that cause $\tilde{G}_{m;[g]}(\mathbf{s}) > 0$. *(ii) Proving asymptotic equivalence:* Assume that existence of a constraint violating policy π , where its cumulative reward is given by

$$\mathbb{E} \left[\sum_{g=1}^G \gamma^{g-1} \{ \mathbf{r}_{m;[g]}(\mathbf{s}, \mathbf{a}) - \tilde{\alpha}(g) \tilde{\mathcal{Y}}_{m;[g]} \} \mid \pi \right]. \quad (91)$$

We compare it with the optimal strategy π^* that satisfies the constraints: for any state $\mathbf{s}_{m;[g]}$ and policy π that violates constraints, when $\tilde{G}_{m;[g]}(\mathbf{s}) > 0$, the penalty $\tilde{\alpha}(g) \cdot \tilde{G}_{m;[g]}(\mathbf{s})^2 > 0$ will increase with $\tilde{\alpha}(g) \rightarrow +\infty$, making the accumulated reward decrease. Therefore, when having $\tilde{\alpha}(g) \rightarrow \infty$, the expected cumulative reward of any policy π that violates the constraint will be significantly reduced, that is:

$$\mathbb{E} \left[\sum_{g=1}^G \gamma^{g-1} \{ \mathbf{r}_{m;[g]}(\mathbf{s}, \mathbf{a}) - \tilde{\alpha}(g) \tilde{\mathcal{Y}}_{m;[g]} \} \mid \pi \right] \rightarrow -\infty. \quad (92)$$

As a result, only those strategies that satisfy constraint $\tilde{G}_{m;[g]}(\mathbf{s}) \leq 0$ can avoid this infinite penalty and ensure that the cumulative reward does not tend towards negative infinity. *(iii) Whether the optimality of the strategy is consistent with the original function:* According to (ii), it can be concluded that in the policy set where the constraint $\tilde{G}_{m;[g]}(\mathbf{s}) \leq 0$ is strictly satisfied, we have

$$\max(\tilde{G}_{m;[g]}(\mathbf{s}), 0)^2 = 0. \quad (93)$$

This indicates that the cumulative reward, which includes a penalty term, is equivalent to the original cumulative reward

function. This is because the penalty term vanishes for states $\mathbf{s}_{m;[g]}$ that satisfy the constraint, leaving the reward function unchanged. Therefore, the optimality of strategies in this constrained policy set is consistent with the optimality derived from the original cumulative reward function in (87).

Based on the above three aspects, we have proven that the cumulative reward with a penalty term is equivalent to the original cumulative reward. Thus, in the set of policies that satisfy constraints, the optimal policy $\tilde{\pi}$ should be equivalent to π^* because they both maximize the original cumulative reward.